The Hong Kong Polytechnic University

THERMOELECTRICITY OF SMALL-MOLECULAR-WEIGHT ORGANIC SEMICONDUCTORS AND TITANIUM OXIDE NANOTUBES

Hu Wenhao

Master of Philosophy

2011

THE HONG KONG POLYTECHNIC UNIVERSITY

DEPARTMENT OF MECHANICAL ENGINEERING

THERMOELECTRICITY OF SMALL-MOLECULAR-WEIGHT ORGANIC SEMICONDUCTORS AND TITANIUM OXIDE NANOTUBES

by

Hu Wenhao

A thesis submitted in partial fulfillment of the requirements for the degree of Master of Philosophy

September 2010

Certificate of Originality

I hereby declare that this thesis is my own work and that, to the best of my knowledge and belief, it reproduces no material previously published or written nor material which has been accepted for the award of any other degree or diploma in any other University or Institute, except where due acknowledgement and reference have been made in the text of the thesis.

__________________ **(Signed)**

__________________ **(Name of Student)**

Abstract

In this present study, the thermoelectric effect of small-molecular-weight semiconductors and titanium oxide nanotubes has been studied. In thesis studies, the thermoelectric effect is employed as both a characterization method and a target for enhancement by structural modification. The characterization of the effective channel thickness of an organic field effect transistor entails the need for a non-destructive characterization that precisely describes the expansion and shrinking of the channel in response to different operation gate voltages. Based on the Boltzmann Transport Theory, the correlation of the Seebeck coefficient with the charge carrier transport properties, including the areal and volumetric carrier density, the effective density of states, the threshold voltage, and the gate voltage can be numerically derived. The data of the series of experiments conducted in this study have shown that the charge carrier density can be effectively modulated by external fields created by the imposed biases on the gate of the OTFTs, and the carriers tend to concentrate close to the dielectric interface when the field effect is enhanced. The concentration profile deviates from the Debye length prediction because of the layer-by-layer deposition nature of the organic semiconductor molecules. These results are used in evaluating the effective channel thickness of the OTFTs under different operating bias, which can be very useful in production-related applications. In such applications, the film thickness of the channel can be precisely controlled by the effective channel thickness predicted by this method. For titanium oxide nanotubes, the measurement of thermoelectric properties follows the similar scheme, but the focus is on

the enhancement of the thermoelectricity of titanium oxide. The Seebeck coefficient of the nanotubes with different annealing conditions are measured and compared. Besides the general trend of the enhancement of Seebeck coefficient by annealing temperature, an interesting change of sign in the Seebeck coefficient is found in the samples annealed in vacuum. The result have shown that the thermoelectric properties of the titanium oxide can effectively be enhance by introducing nanotube structures, and that due to the introduction of extra oxygen vacancies, both the morphology and the thermoelectric properties demonstrates close relationships, especially those annealed in high vacuum environment. The results of this study can serve as a foundation based on which further improvements can be made on the thermoelectric measurement, enhancements and effective-channel-thickness related applications. The relative convenience and precision of this tool is effectively an advantage of thermoelectric effect measurements.

Acknowledgements

First and foremost, I would like to give my appreciation to my Chief supervisor, Dr. Paddy Kwok Leung Chan and co-supervisor, Prof. San Qiang Shi for their support and patience on my study in the past two years. The guidance and meticulous instructions from them have greatly improved my research methodologies and endowed me with a good background based on which my future career path can effectively unfold. I would also like to thank Dr. Chi Wah Leung for his help in clarifying many concepts for me in accomplishing this work.

My thanks also go to my senior lab fellows, Dr. Su Mei Wang, Mr. Jing Chuan Wang, who helped me in the fabrication process and gave me lots of ideas in controlling the fabrication parameters so that my experimental results would not be affected by some external factors. Besides that, their enlightening conversations with me and serious research attitudes are also what I highly appreciate. Mr. Anthony Leung, the undergraduate research assistant, also help me a lot in experimenting with different temperature combinations in the three-zone furnace to find out the best for the purification of the organic semiconductor materials. I would also take this opportunity to express my gratitude to Mr. Yeung of the Materials Research Center (MRC) of Hong Kong Polytechnic University. His patient hands-on instructions on the use of Scanning Electron Microscopy (SEM) and Atomic Force Microscopy (AFM) have granted me with the ability to scan my samples experimentally.

Finally, I would like to thank my family for their support in the past two years of my lab life. My father, mother and my fiancé lived in Shanghai, far away from Hong Kong, but they still managed to come here to see me every couple of months. My parents had to spare much time from their busy administrative duties in their companies to make this happen, and my fiancé even managed to find a job in Hong Kong so that we can live together. Their whole-hearted, selfless and continuous support has made my life in Hong Kong much easier than it was otherwisely, and my research study considerably more effective and efficient. Thanks once again!

Table of Contents

List of Figures and Tables

1. Introduction

1.1 Thermoelectric effect and Seebeck coefficient

Thermoelectric effect is based on the Zeroth Law of Thermodynamics, which states that thermal equilibrium can be achieved on any two systems upon thermal contact. The thermoelectric effect converts temperature differences to electric voltages and vice versa. A voltage can be induced in a thermoelectric device when it is exposed to an inside temperature difference, and reversely, a temperature difference can be created when a voltage is applied on the device. Just like the gas’s expansion when it is heated, the charge carriers in the material – including electrons or holes - diffuse from the hot side to the cold side. Such thermally induced carrier diffusion will establish an electric field within the material, and the diffused carriers are balanced by the drifted carriers at equilibrium. Hence, a thermally-induced electric potential, called thermoelectric voltage, is produced between the hot end and the cold end, and when these ends are connected via external circuit, a basic thermoelectric device is made. Since the thermoelectric voltage is usually rather small within a limited range of temperature difference, simple thermoelectric devices are usually connected in series. This type of devices can vary in forms, dimensions and materials, but the basic structure can be illustrated in Figure 1, which covers the two modes of thermoelectric effect applications. The diagram on the left illustrates the power generation mode, while the diagram on the right illustrates the cooling/heating mode. The power generation mode utilizes the thermoelectric effect to convert thermal energy to electric energy, and the cooling/heating mode does the reverse conversion. Both modes can be based on the same device structure, which is comprised of primarily two semiconductors with reverse type. The dominant charge carrier is electron in the N-type semiconductor and hole in the P-type semiconductor. When they are linked head to tail by three electrodes as shown in the figure, a thermoelectric voltage can be obtained upon a temperature difference, because both types of carriers tend to diffuse from the hot side to the cold side. In cooling/heating mode, however, the direction of energy conversion is reversed, where the carriers are driven by the external electric field and their movement along the electric field contributes collectively to the heat transfer from one side to the other, building up a temperature difference.

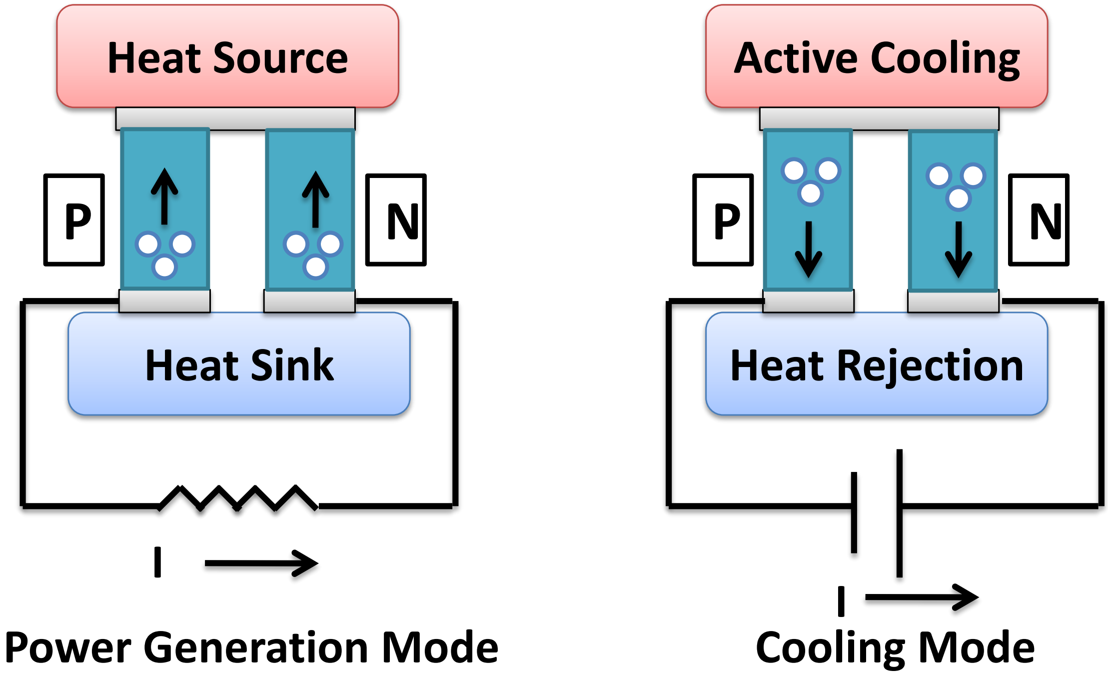

Figure 1 Schematic illustration of thermoelectric effect. The left configuration illustrates the power generation mode, where electricity is produced upon a temperature difference; the right configuration illustrates the cooling/heating mode, which utilizes the thermoelectric device, known as a Peltier module, to transfer heat energy from one end to the other. Both illustrations are based on parallel connection in which an N-type semiconductor is placed parallel to a P-type one in order to establish a circuit.

To quantitatively evaluate the capability of a material to convert temperature difference to thermoelectric voltage as well as the reverse scenario, Seebeck coefficient (S) was introduced. The Seebeck coefficient of a material measures the magnitude of an induced thermoelectric voltage (ΔV) in response to a temperature difference (ΔT) across that material. It can be calculated by the simple equation $S = \frac{\Delta V}{\Delta T}$, which is simply a division of the thermoelectric voltage by temperature difference. It can be seen that higher S corresponds to higher thermoelectric voltage obtained with the same temperature difference, and a higher temperature difference when the same voltage is input. The value of S varies from material to material and has a range in the order of several μV/K to several hundred μV/K for most materials. Seebeck coefficient can also be negative or positive, depending on the primary charge carrier in the material. Table 1 shows S of some typical metals and semiconductors at room temperature (RT). These values are nevertheless not exact values because they are subject to the variation of the actual testing environments, of which temperature is an important factor. Typically speaking, metals have relatively small Seebeck coefficients while semiconductors have larger values.

Metal	Seebeck Coefficient	Semiconductor	Seebeck Coefficient
	μV/K		μV/K
Copper	6.5	Se	900.0
Silver	6.5	Te	500.0
Gold	6.5	Si	440.0
Tantalum	4.5	Ge	300.0
Aluminum	3.5	PbTe	-180.0
Nickel	-15.0	n-type Bi_2Te_3	-230.0
Bismuth	-72.0	p-type Sb_2Te_3	185.0

Table 1 Seebeck coefficients of some typical metals and semiconductors at room temperature (RT)

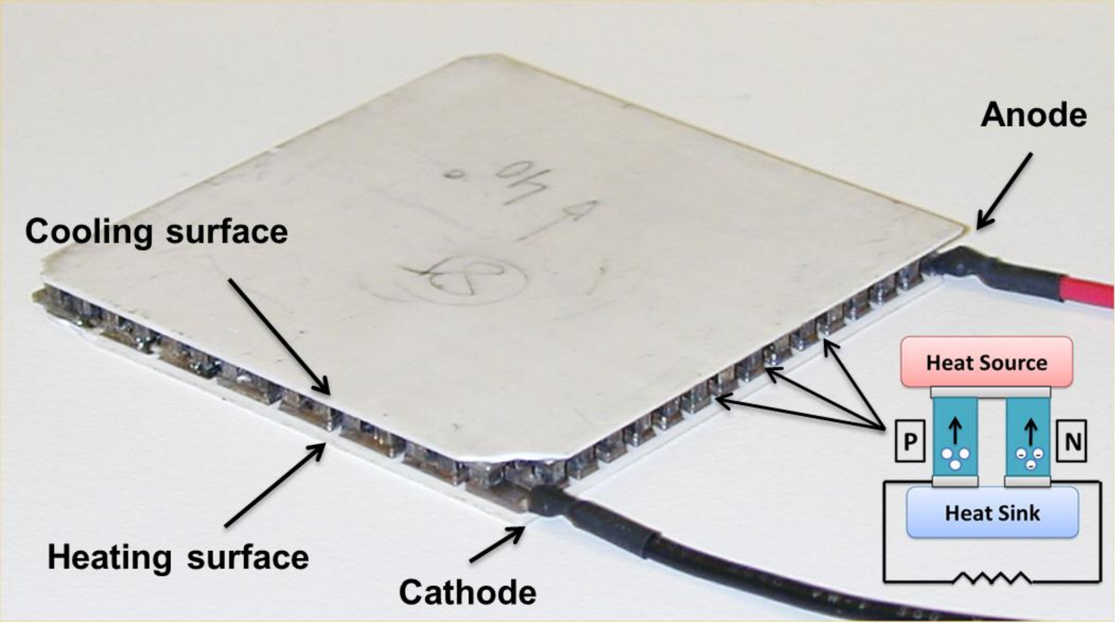

Figure 2 A thermoelectric cooler, or Peltier cooler, made of Bi_2Te_3, is comprised of numerous thermoelectric "elements" in series, with each end thermally connected by ceramic covers.

In solid state physics viewpoint, the thermoelectric effect is based on the fact that highly energetic carriers scatter off low-energy lattice atoms and deposit energy in vibration modes, while phonon scattering contributes likewise to increased carrier density. The energy level at which electrical carriers are in equilibrium with the surrounding lattices varies according to both the material composition and the equilibrium temperature.[1] Macroscopically, Seebeck coefficient is a measure of the magnitude of an induced thermoelectric voltage in response to a temperature difference across that material, and it can be either positive or negative both in metals and in semiconductors, as shown in Table 1. In metals, the energy bands are usually half-filled, making electrons and holes, which have opposite charge signs, canceling each other in their the contribution to the thermoelectric voltage. Therefore, the total Seebeck coefficient is typically small. In comparison, the concentration of electrons and holes in semiconductors are usually incomparable, making one of them dominate the charge transport inside the material. The excess electrons or holes have varied contribution to the Seebeck coefficient when the semiconductor is doped with different level of impurities, and can be either negative or positive depending on the charge type of the excess carriers.

1.2 Seebeck coefficient measurement as a method to study carrier transport properties

Besides the usefulness of Seebeck coefficient, or thermopower, in evaluating the potential of a material in thermoelectric applications, it is also a well-established parameter based on which studies on some fundamental charge-transport-related parameters can be conducted. It has a strong link with the Fermi energy, the charge carrier concentration and the scattering mechanism, all of which are fundamental parameters associated with the macroscopic physical properties like the electrical conductivity and the thermal conductivity. Quantitative connection can be derived among these fundamental parameters based on a few plausible assumptions. For instance, when the scattering of the current carriers is contributed by only one scattering mechanism, assuming that Fermi energy only weakly depends on the temperature, and that the lower limit of the conduction band is zero while the upper limit of the valence band equals to the bandgap, the following relationship holds for the non-degenerate semiconductors of n-type and of p-type, respectively: [2]

$$S_n = -\frac{k}{e}(r + \frac{5}{2} - \frac{E_f}{kT}) = -\frac{k}{e}(r + \frac{5}{2} + \ln\frac{N_c}{n}) \qquad \mathbf{1}$$

$$S_p = \frac{k}{e}(r + \frac{5}{2} + \frac{E_f + E_g}{kT}) \qquad \textbf{2}$$

where k is the Boltzmann constant, e is the charge of electron, E_f is the energy of the Fermi level (the energy is measured from the lower bound of the conduction band, E_c), E_g is the energy bandgap, n is the concentration of the electrons, N_c is the density of the states in the conduction band, r is a parameter depending on the nature of the scattering mechanism of the current carriers.[2]

For n-type semiconductor, based on Equation 2, the Fermi energy level can be given by:

$$E_F = e\frac{S_n'' - S_n'}{\frac{1}{T''} - \frac{1}{T'}} \qquad \textbf{3}$$

For p-type semiconductor, based on Equation 3, the Fermi energy level can be given by:

$$E_F = e\frac{S_p'' - S_p'}{\frac{1}{T''} - \frac{1}{T'}} - E_g \qquad \textbf{4}$$

where $T'' - T'$ is a small domain on which r and E_F are independent of temperature. This is essentially taking derivative, meaning the slope of the linear dependence of the Seebeck coefficient against 1/T. The absolute value of Seebeck coefficients presents a linear decrease/increase with the increase of the measurement temperature, which is taken as the average temperature of the hot side reading and the cold side reading in the stabilized region. $T = (T_h+T_c)/2$, where T_h is the hot electrode (in our case the negative electrode) temperature and T_c is the cold electrode (in our case the positive electrode) temperature.

To extract the semiconductors' transport properties, one may also resort to Hall Effect measurement, but one important advantage of doing Seebeck coefficient measurement to study these properties is that it overcomes a major difficulty of conducting Hall Effect measurement. One major disadvantage of doing Hall Effect measurement is that it cannot filter the contribution from an additional highly-conductive degenerate layer created by doping, or a metal substrate, because the interference from the conductive layer diminishes or enhances the field which the Hall probe is supposed to detect, making the results less accurate. Additional problems include the influences of temperature, layer thickness and external magnetic fields. For Seebeck measurement, however, the apparent S is related to the bulk S in the following relationship:

$$S_{apparent} = \frac{\sigma_b}{\sigma_b + \sigma_s} S_{bulk} \qquad \mathbf{5}$$

where σ_b is the electrical conductivity of the bulk non-degenerate semiconductor sample, and σ_s is the thin film degenerate semiconductor or the metal layer on top of the bulk, like the Ti metal substrate beneath the titanium oxide nanotubes that will be introduced later in this report. Since Seebeck coefficient of a doping layer will be significantly smaller than that of the bulk, the sign of the Seebeck coefficient is solely determined by the bulk conduction properties. The sign of the Seebeck coefficient is important as it is a telling parameter for the study of carrier concentration and mobility of the charge carriers in the semiconductor, namely the transport property. Therefore, we must tap into the derivation of such quantities, based on:

$$S_{bulk} = \frac{S_p \mu_p p + S_n \mu_n n}{\mu_p p + \mu_n n} \qquad \textbf{6}$$

where S_p, μ_p, and p are the Seebeck coefficient, the mobility and the carrier concentration of holes, and S_n, μ_n, and n are the Seebeck coefficient, the mobility and the carrier concentration of the electrons. The sign-reversal temperature is directly related to the mobility ratio of the carriers and the carrier density by considering $S_p = S_n$ at the transition temperature.

1.3 Organic thin film transistors (OTFTs) based on small-molecular-weight organic semiconductors

Organic semiconductors have been studied since the late 1940s.[3] Thanks to their lower vacuum requirement, compatibility with flexible substrate, large area fabrication and low manufacturing cost, organic electronic devices such as photovoltaics,[4,5] light emitting diodes,[6,7] transistors[8,9] and memories[10] have constantly attracted great attention from the researchers. Among them, organic transistors are the key elements for the large area flexible displays, non-volatile memories and driver circuits. However, in terms of widely practiced application, the organic semiconductors are lacking. The frontal studies around this type of materials have been intensively focused on the theoretical and experimental studies of the relevant properties and continual enhancement of the device performances. Light emitting diodes based on organic semiconductor materials[11,12] was theoretically and experimentally studied, along with OTFTs [13, 14] and conjugated polymers, [15, 16]. Overall, the considerable improvement in the energy efficiency [17] have captured the research interest of researchers around the world to exploit the possible application of organic semiconductors. Various organic semiconductors, such as polycrystalline pentacene, poly(3-hexylthiophene) (P3HT) and rubrene single crystal, have been employed to fabricate the organic transistors. OTFTs with high performance have already been demonstrated.[18,19,20] Between the two types of contact configurations, bottom-contact organic OTFTs are usually more desirable in small electric circuit applications, because the lithography techniques used in these applications involve solvents exposure that is destructive to organic semiconductors. But the high contact resistance of bottom contact OTFTs limits their device performance, as demonstrated in Ref.[21].

1.4 Enhancement of thermoelectric figure of merit for organic semiconductors

Besides the potential applications in organic transitors, semiconductors based on organic materials is also a subject for recent intense investigations in reaching high electronic performance. This is because of the importance of charge carrier transport inside organic semiconductors to the performance of organic electronic devices. Recent investigations in the Seebeck coefficient of pentacene thin film and rubrene single crystals were conducted and the Seebeck coefficient of field-effect devices at the temperature between 295K and 200K have been obtained.[22,23] The measured Seebeck coefficient falls into the range of $0.3 - 1\ \mathrm{m \cdot V \cdot K^{-1}}$, and decreases logarithmically with increasing gate voltage. Earlier measurements on thermal transport properties in pentacene thin films and rubrene single crystals show room-temperature thermal conductivities of the order of $0.5\ \mathrm{W \cdot m^{-1} \cdot K^{-1}}$.[23, 24] These results have shown genrally large Seebeck coefficients and small thermal conductivities, indicating that organic semiconductors can potentially be good thermoelectric materials.[23]

However, current applications of thermoelectric coolers and heaters are limited by the efficiency of their thermal-electrical conversion. The parameter to evaluate the efficiency of the conversion is called thermoelectric figure of merit, $ZT = S^2\sigma T/\kappa$, where S is the Seebeck coeffient, σ being the electrical conductivity, T being the temperature, and κ is the thermal conductivity. Therefore, it is appraent that in order to have a highly efficient thermoelectric device, the material should have large Seebeck coefficient and electrical conductivity, while simutaneously maintaining small thermal conductivity. However, it is not easy to find a material with all the above parameters optimized, due to the fact that Seebeck coefficient, electrical conductivity and thermal conductivity are interconnected. The defining parameters behind them are carrier concentrations, effective mass of charge carriers, and the electronic κ_e and lattice κ_L thermal conductivities, whose addition yields the total thermal conductivity.

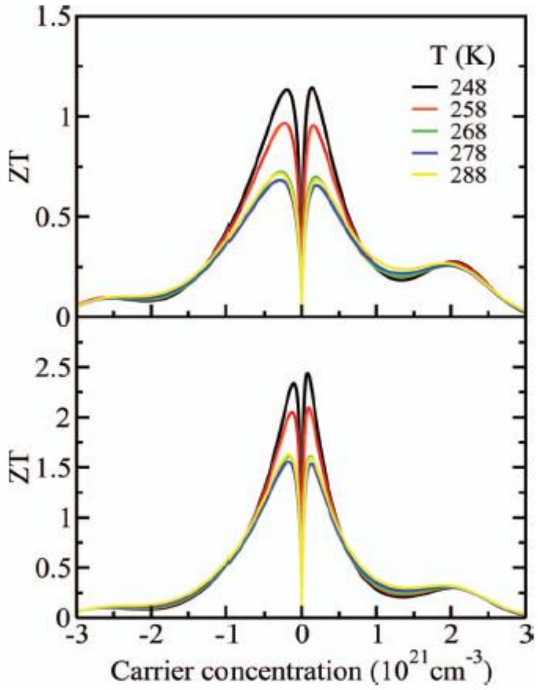

Figure 3 first-principles caulculation to study the potential ZT of pentacene with regard to carrier concentration. based on the calculated transport coefficients along the a crystal direction and is derived from the temperature dependence of mobility =11.2 (upper panel) and 35 cm^2 /V^{-1} s^{-1} (lower panel) at room temperature, respectively.

(Source: Wang *et al* First-principles investigation of organic semiconductors for thermoelectric applications, The Journal of Chemical Physics **131**, 224704 (2009))

By applying the first-principles electronic structure calculations coupled with the Boltzmann transport theory, Wang *et al* had studied the thermoelectric effects in organic semiconductors.[23] In their efforts, the absolute value of the Seebeck coefficient in pentacene and rubrene in the constant relaxation time approximation is obtained. For pentacene, the peak ZT value falls in the range of 0.8–1.8 at 294 K and 1.1–2.4 at 248 K[23] In terms of figure of merits, these values are highly attractive as most commecially used thermoelectric materials exhibit similar, if not lower, ZT values. Because the environmental-friendly nature of the organic semicondcutors, the potential of using them as the thermoelectric materials for room temperature applications is far-reaching.

2. Evaluation of the Effective Channel Thicknesses of Organic Thin Film Transistors by Thermoelectric Effect

2.1 Introduction

The transport of charge carriers and the transfer of energy in the organic semiconductor are closely related to the operation of organic electronic and optoelectronic devices. Understanding the nature and dynamics of charge carriers in this special class of electronic materials has been at the focus of intense research efforts. Typically for organic semiconductors, such as rubrene ((5,6,11,12-tetraphenylnaphthacene) and pentacene ($C_{22}H_{14}$), electronic transfer integrals are expected to be small, electron–phonon coupling strong, and scattering of charge carriers very efficient.[25] In fact, these basic transport mechanisms are not only of fundamental academic interest, but also bear great technical relevance in that more professional knowledge may help to increase transport efficiency with the consequences of increased device speed, reduced power loss and avoidance of excessive heating in such promising fields as pixel-resolved full color organic light emitting diode (OLED) displays, organic field effect transistor (OFET) integrated circuits, or photovoltaic cells.[25]

However, many fundamental carrier-tranport-related parameters of organic semiconductors, highly important in the design of efficient electronic and optoelectronic devices, are still insufficiently comprehended. One example is the distribution of charge carriers across the accumulation layer when field effect is applied, which is associated with the field-effect induced mobility degradation phenomenon.[28] This phenomenon is symbolized by decreased mobility with increasing gate voltage, and can be explained via the charge carrier distribution mechanism. However, the charge carrier distribution within the organic accumulation layer has yet to be experimentally studied. In order to do so, it is helpful to bring in the Seebeck coefficient measurement. As a basic transport property of solids, the Seebeck coefficient provides a deep insight into the carrier concentrations and Fermi energy. In this chapter, efforts are focused on the measurement of the carrier-density-dependent Seebeck coefficient in organic semiconductors by using field-effect-based device structures. By employing varied gate voltage to modulate the Seebeck coefficient, the volumetric carrier concentration within the channel can be obtained. Subsequently, by combing the volumetric carrier concentration with the areal carrier concentration, the effective channel thickness, which reflects the extent to which carriers concentrates at the organic-dielectric interfaces, is derived. Finally, the optimal contact thickness of bottom contact OTFTs under the operating voltage range of the device, can be suggested based on the effective channel thickness.

2.2 Effective Channel Thickness in OTFT

The carrier-density-dependent Seebeck coefficient is essentially a paraphrase of the variable S modulated by the field effect. The charge carrier concentration, or charge carrier density, denotes the number of charge carriers per unit volume, and has the unit of m^{-3}. The modulation of S is useful in multiple applications, among which the determination of the optimal contact thickness in bottom contact organic OTFTs is an important one. This is achieved via the characterization of the effective channel thickness, that is, the thickness of the organic-monolayer-based channel that contributes directly to the accumulation/depletion of the carriers in OTFT operation.

In OTFTs, it had been shown that only a few organic monolayers are sufficient for proper transistor operation.[26] The word "sufficient" means that a certain number of layers can help the device achieve the highest carrier mobility (μ), and further increase of monolayer numbers only decreases the mobility or make no difference. The mobility of the OTFTs plays an important role in governing the operating current and frequency, and thus the device performance. Usually, one can evaluate the mobility of an organic transistor by the equation commonly adopted for the inorganic semiconductor transistors,[27]

$$I_{DS} = \frac{WC}{2L}\mu(V_G - V_{th})^2 \qquad \mathbf{7}$$

where I_{DS} is the drain source current, V_G is the gate voltage bias and V_{th} is the threshold voltage, respectively. For inorganic semiconductors, the field effect ($|V_G|>0$) mobility of the carriers within the accumulation region (channel) is usually smaller than the bulk carrier mobility due to various scattering effects such as dielectric surface roughness, surface phonons and impurities.[11] Similar mobility degradation effect has also been observed by Horowitz *et al.* in the organic transistors with alumina dielectric materials. They found that the mobility drops more significantly as a function of $|V_G-V_{th}|$ in the pentacene/Al_2O_3 devices than the pentacene/SAM/Al_2O_3 device,[28] and applied the multi-layer model (MLM) to study the carrier distribution along the channel at varies gate biases. The model suggested that the induced carriers mainly accumulated at the first one to two monolayers (MLs) of the organic semiconductor next to the dielectric materials at large gate bias, as shown in Figure 4. The figure shows a narrowing of distribution profile from more than 10MLs to just 1 to 2 MLs when the gate voltage increases from 1V to

10V. Because of the concentration of carriers in large gate voltages, it is inferred that the carrier mobility of the channel is limited by the traps, defects, and arrangement of the organic molecules on the first few monolayers of the organic semiconductor.[12]

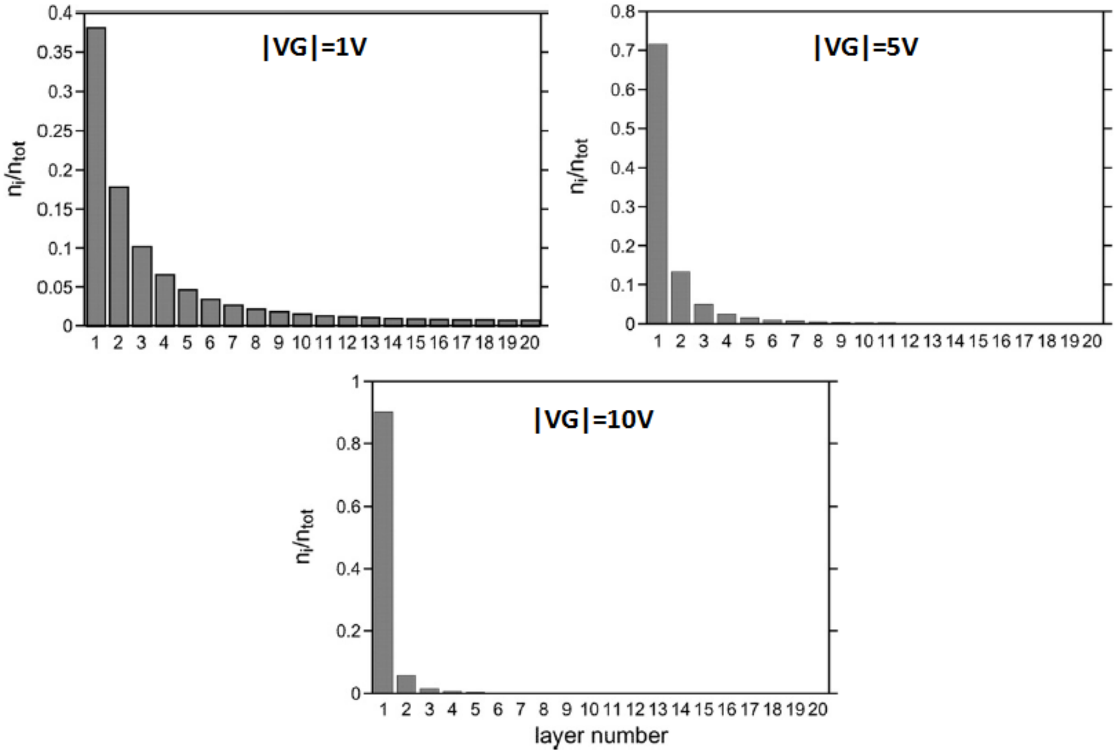

Figure 4 Distribution of charge carriers in a 30nm thick pentacene film with an insulator capacitance of 75nF/cm^2. Gate voltages of 1V, 5V and 10V yields increasingly concentrated charge carriers to the first few monolayers.

(Source: M. Mottaghi, G. Horowitz, Organic Electronics 7 (2006) 528–536)

In light of its usefulness in exploring the gate voltage dependent mobility degradation effect, the impact of the number of the first few monolayers on the channel conduction was experimentally studied by Yoneya *et al.* The primary target of their research effort is to study the contact-resistance-dominated channel conduction, but while they varied the Au thickness in a Ti/Au electrode configuration, it was found that the conduction is related primarily to the first 3nm of the pentacene organic thin film at V_G=-10V, as shown in Figure 5. In Figure 5 (a), the contact resistance is found to initially increase with the Ti thickness, but clamped at 3nm. The reason is explored and presented in two illustrative diagrams Figure 5 (b) and (c). Since effective conduction between the pentacene and the contacts is primarily realized via the Au-pentacene interface, rather than the Ti-pentacene interface which has a significant HOMO – work function mismatch. It was deduced that the conduction happens only after the Ti layer decreases lower than 3nm, allowing more conduction through Au. Based on this result, it was estimated that the effective channel thickness of their pentacene OTFT is ~3nm for V_G=-10V, and electrodes higher than that level were not found to have any effect in enhancing the conduction anymore.[29]

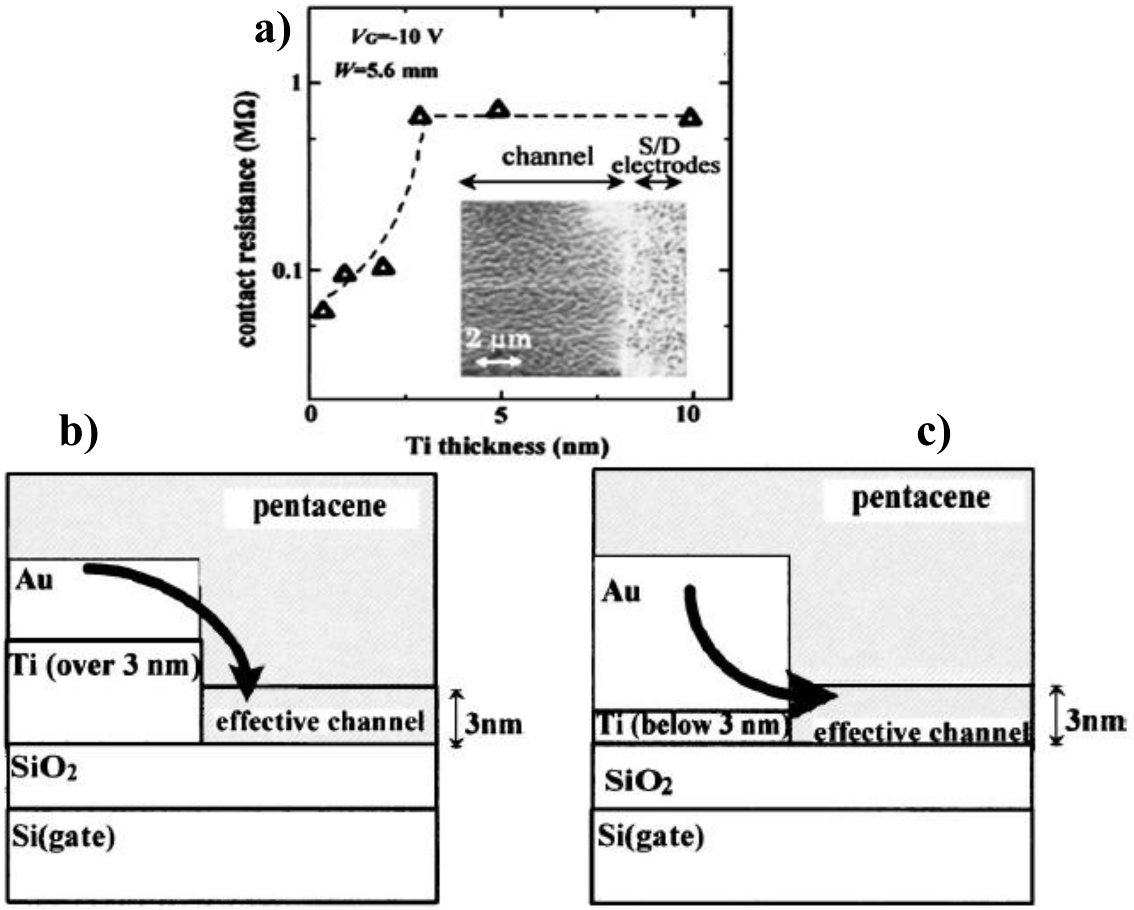

Figure 5 Contact resistance of the pentacene OTFTs clamps as the Ti thickness increases, as shown in a). The mechanism of the clamping is explained by the effective channel thickness, which is ~3nm at VG=-10V. At Ti over 3nm (b)), the conduction is suppressed; at Ti below 3nm (c)), the conduction proportionally increases with the contact area between the gold electrode and the effective channel.

(Source: N. Yoneya, M. Noda, N. Hirai, K. Nomoto, M. Wada, J. Kasahara, *Appl. Phys. Lett.* **85**, 20, (2004))

2.3 Optimal Contact Height in OTFT as Characterized by Seebeck measurement

One of the potential applications of studying the effective channel thickness is the determination of the optimal contact height in bottom contact OTFTs. In organic light-emitting diodes driven by organic thin film transistor on plastic substrates,[30,31] finding such an optimal electrode thickness in their operating gate voltage range would be an attractive direction, because display applications require the OLED-controlling circuitry to be as transparent as possible. It is even better if the effective channel thickness at different gate voltages can be found, so that the contacts can be fabricated to maximize mobility within the whole application range. Generally speaking, an electrode thickness that is not only thin enough to ensure good transparency but also thick enough to ensure good device performance, which impacts the contrast ratio, is most desirable. This is shown schematically in Figure 6, where three representative working modes of the controlling OTFT are explored. As can be seen, the low power mode, which corresponds to a large effective channel thickness, sets the boundary condition for the contact thickness. As long as the contact is thick enough to meet the operating need of the lowest power mode, good mobility throughout the whole operating range can be ensured.

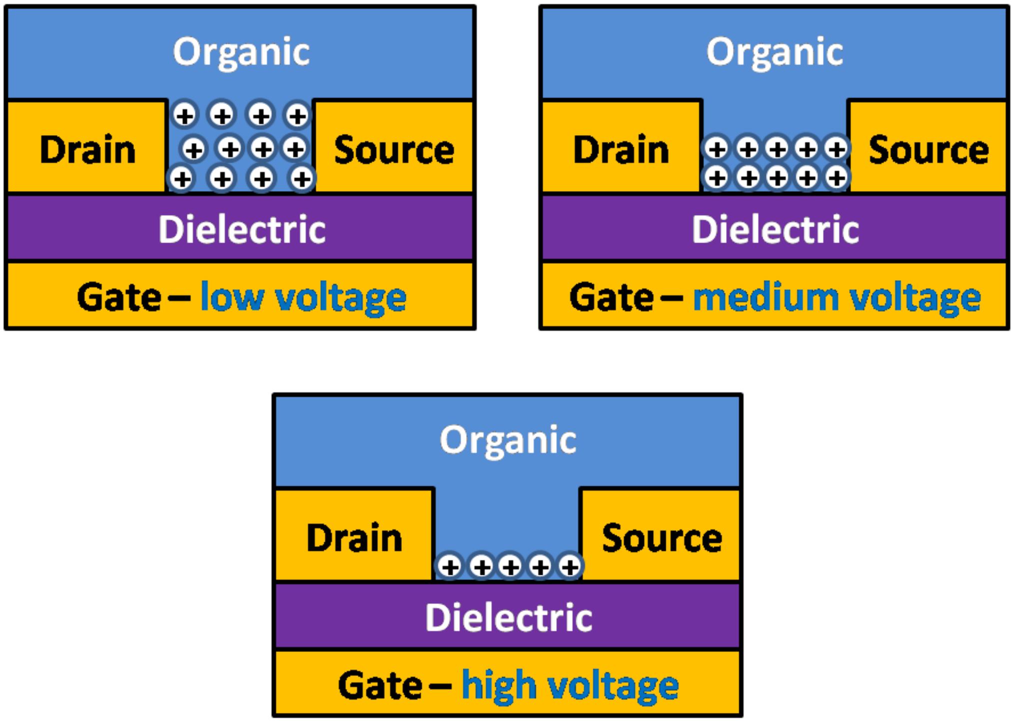

Figure 6 Illustration of potential application for optimal contact height determination. In the low power mode (upper left), medium power mode (upper right), and the high power mode (bottom), the effective channel thickness decreases with increasing gate voltage. The effect channel thickness in the low power mode corresponds to the maximum contact thickness as needed.

However, the contact height is not the only factor that affects the device performance. It has been reported that the morphology of the first few monolayers also affects the bottom contact OTFTs' devices performance to a great extent. Mun *et al* confirmed this impact in their study on pentacene OTFTs based on different gate insulators.[32] Pentacene samples on hydrophobic dielectric show a significant ramp of drain current as the organic film becomes thicker (from 15nm to 50nm), while the drain current in samples on hydrophilic dielectric gradually drops with thickness. Therefore, the mobility of the pentacene OTFT changes against pentacene film thickness in dramatically different ways as shown in Figure 7 (d) and Figure 8 (d). They found the variation of the drain currents are caused by the different morphologies of the organic thin films. Smaller grain sizes and larger surface roughness (defined by peak-to-valley height in AFM test) of the samples on the hydrophobic dielectric leads to generally smaller drain current than those on the hydrophilic dielectric, and this difference becomes pronounced only when the film thickness is small enough (such as 15nm, as shown in Figure 7 (a) and Figure 8 (a)), because at such thickness the large surface roughness of the hydrophobic samples begins to impair the channel interconnection in the first few pentacene monolayers where carrier concentration is highest.[32] However, two uncertainties may affect the accuracy of this AFM-based channel characterization: 1) The morphology of the first few monolayers cannot be characterized by the AFM test, particularly for thicker organic films where the interfacial layers are entirely covered by the surface layers. 2) The peak-to-valley surface roughness cannot reflect the actual channel conduction as it is contributed by both the completed organic monolayers and the islands on the top. An equivalent – or effective – conduction channel thickness, which quantitatively accounts for the differences in drain currents, is lacking in such an analysis. Furthermore, AFM test is not suitable for large scale device quality inspection because it may cause destruction to the sample and cost long measurement time.

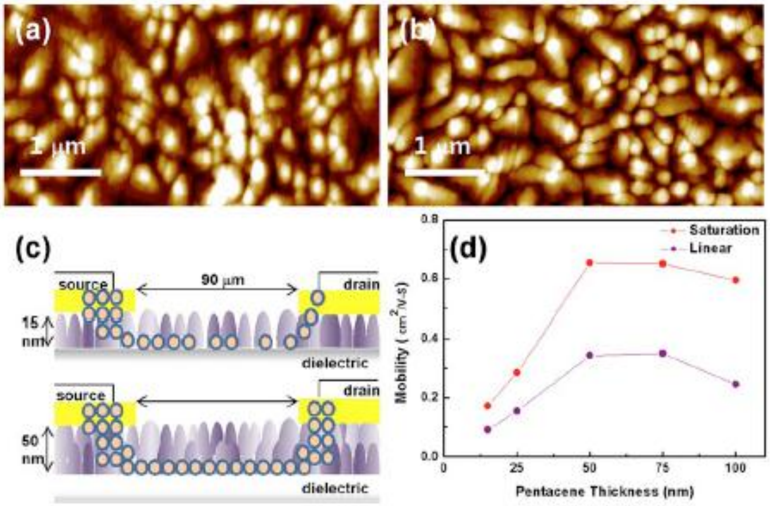

Figure 7 AFM images of a) 15-nm-thick and b) 50-nm-thick pentacene channel layers grown on hydrophobic PVP dielectric. c) Schematic illustration of the hole transport happening on the 15-nm-thick and the 50-nm-thick OTFTs. d) Saturation and linear mobilities as a function of pentacene film thickness

(Source: S. J. Mun, J. M. Choi, K. H. Lee, K. Lee, S. Im, *Appl. Phys. Lett.*, **93,** 233301, (2008))

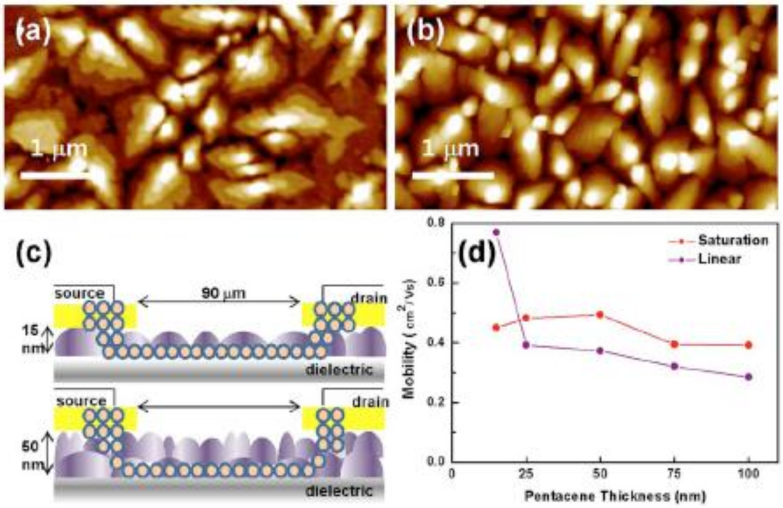

Figure 8 AFM images of a) 15-nm-thick and b) 50-nm-thick pentacene channel layers grown on hydrophilic PVP dielectric. c) Schematic illustration of the hole transport happening on the 15-nm-thick and the 50-nm-thick OTFTs. d) Saturation and linear mobilities as a function of pentacene film thickness

(Source: S. J. Mun, J. M. Choi, K. H. Lee, K. Lee, S. Im, *Appl. Phys. Lett.*, **93,** 233301, (2008)) To address the uncertainties as mentioned above and to evaluate the optimal contact height of the bottom contact OTFTs, thermoelectric measurement technique is proposed and employed. In this chapter, it is used to experimentally characterize the effective channel thickness of organic thin film transistor as a function of gate bias. Thermoelectric effect is closely associated with carrier transport properties including charge carrier concentration, Fermi energy and scattering mechanisms, and it provides effective insights into the carrier distribution within the channel. It is also a non-destructive method for device characterization, and thus a suitable candidate for characterizing the channel conduction properties for organic thin film transistors. Furthermore in this chapter, the effective channel thickness, obtained by the volumetric and areal carrier concentration, will be compared with the Debye length, which is the distance over which significant charge separation can occur. The effective channel thickness obtained by this method has taken into account the collective contributions from both the complete film and the islands on the top, and would be useful in determining the minimum contact height in bottom contact OTFTs with different ranges of operating gate voltages.

Two types of devices are studied in this chapter, one being rubrene bottom contact OTFTs and the other pentacene top contact OTFTs. Pentacene thin film is currently under intensive research efforts for its highest achievable filed-effect mobility among other organic material based thin film transistors.[33] Regarding the device structure, one reason to choose top contact structure for pentacene OTFT is because of the self-assembly-monolayer (SAM) required for well aligned pentacene molecules to develop on the dielectric. It increases the difficulty of making a bottom contact pentacene OTFT because the solvent for SAM treatment causes damages to the metal electrodes. Top contact structure is chosen also because of demonstrations in several experiments conducted on bottom contact OTFTs.[34] Nucleation of pentacene is found to take place preferentially at the electrodes or the area near the electrodes, causing discontinuities and clustering in the pentacene film.[35] Such discontinuities may induce extra sources of sample-to-sample variations to this study.

2.4 Fabrication and Measurement of Bottom and Top contact OTFTs

2.4.1 Source materials purification

The organic material purification setup, as illustrated in Figure 9, comprises primarily of a long quartz tube inside a horizontal three-zone furnace. Inside the quartz tube are 8~10 similar tubes with smaller length and diameter, one of which is sealed on one end serving as the source boat. One end of the large quartz tube is also sealed and installed with a pressure gage, while the other end is connected with a two stage pumping system consisting of a rough pump and a turbo-molecular pump. Reynolds number in the setup is carefully controlled to ensure laminar flow is fully developed inside the work tube. The source materials are put in the small tube which resides in the region of the highest temperature, usually the 2nd or the 3rd tube. The ends of each small tube are polished to ensure its complete contact with the ones on its left and right sides. All powders are heated a little over its sublimation temperature under respective pressures.

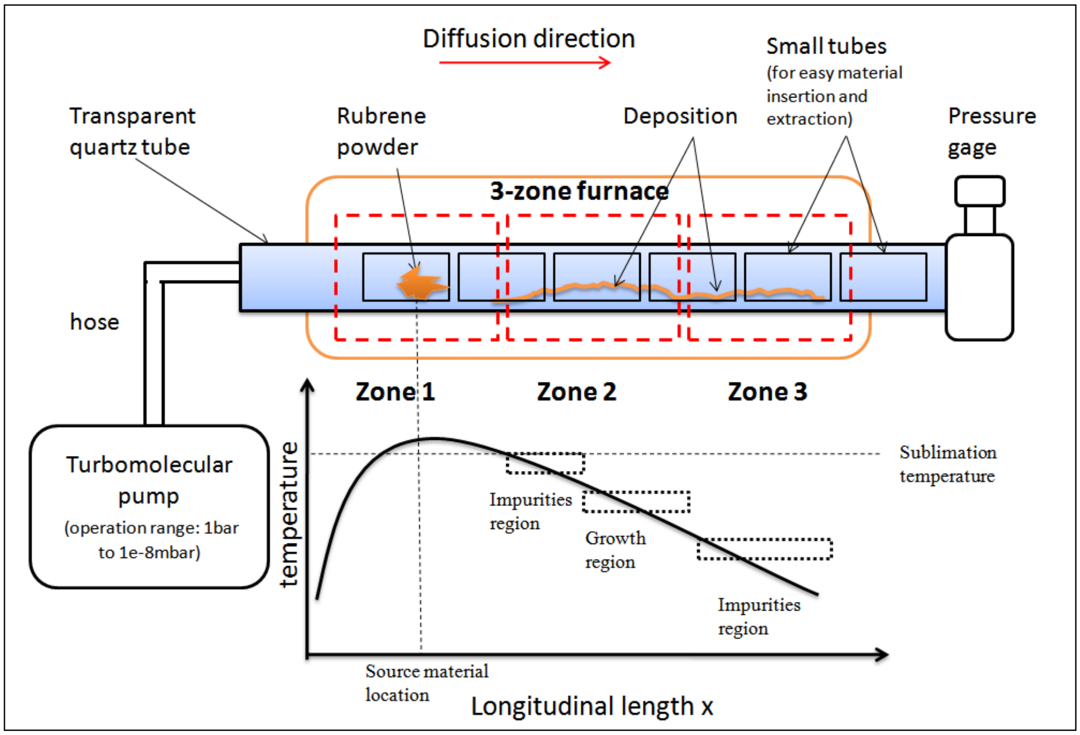

Figure 9 Rubrene purification at high vacuum: the rubrene vapor particles are vaporized at the source region where the temperature is kept slightly higher than the sublimation; pressure will be kept low by a one-stage turbomolecular pump; the temperature distribution is maintained by the 3-zone furnace so that the temperature gradient at the growth region is 1~2K/cm; narrow tubes are placed inside the growth tube for easy material insertion and extraction. The driving force of rubrene evaporant is supplied by diffusion.

Temperature profiles are measured by thermocouple on priori. The three-zone temperatures used in this growth scheme are 220°C, 180°C and 160°C, respectively. The ultimate pressure of 1×10^{-5}Torr is reached before the heating process begins. Lastly, the temperature ramping rate is set at 3°C/s to avoid temperature overshooting or fluctuation. The whole process of rubrene purification is repeated three times before it is used to grow rubrene single crystals. Figure 10 shows a three-zone furnace and the purfication results The three-zone furnace is used to supply temeprature gradient in order to separate impurities to the pure rubrene powder. Both ends show some rubrene deposition due to suddenly droped temperature gradients there. In the center region that corresponds to the growth region and the impurities regions in Figure 9, the rubrene distrbution is shown in the inset on the upper right corner. The heavy red region toward the left end are the relatively pure regions that are collected for the subsequent stage of purification.

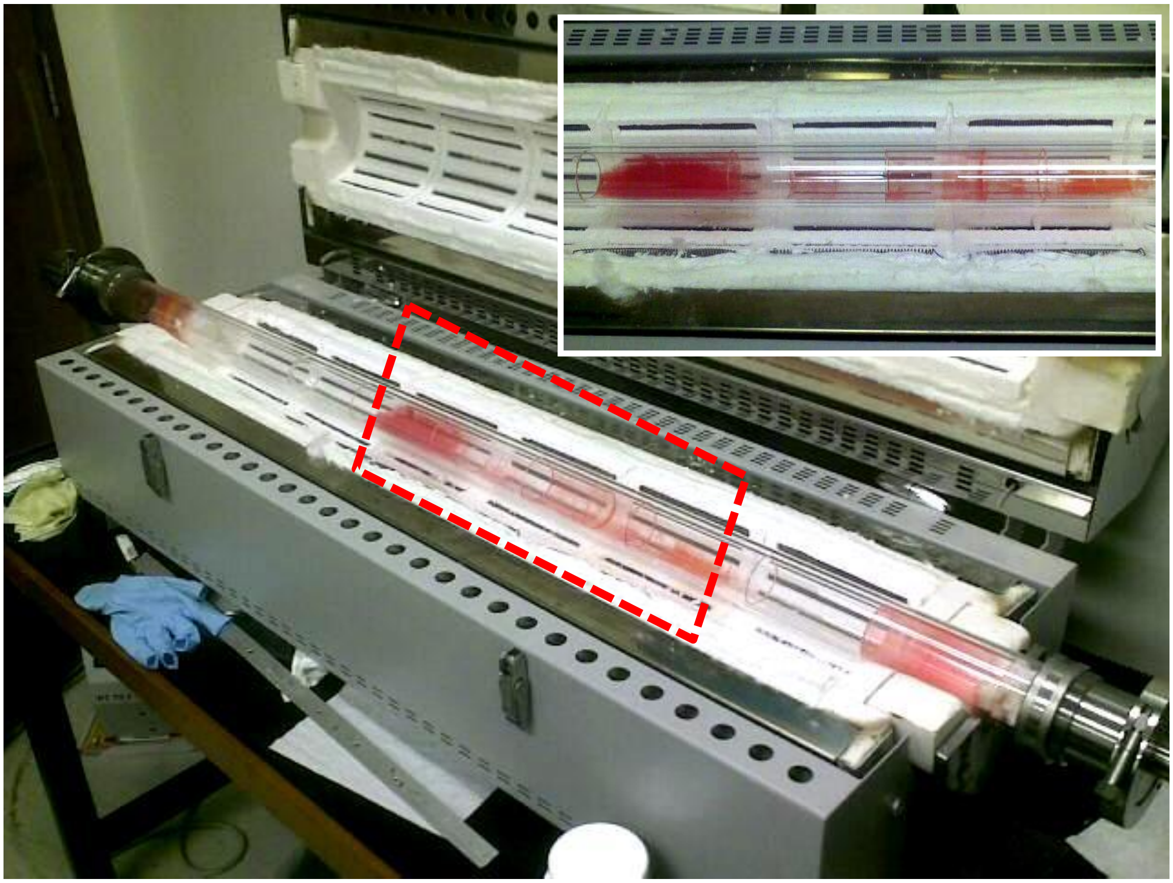

Figure 10 Rubrene distribution after the first of the three purification stages under vacuum condition in the three-zone furnace. The dark red region is collected for the next phase of purification.

2.4.2 Fabrication of Organic Thin Film Transistors

The bottom-contact rubrene thin film transistors are fabricated on heavily doped n-type silicon substrates (<0.005 Ω·cm) with 300nm thermal silicon dioxide as the gate insulator. 50nm thick silver source and drain top contacts are deposited using a shadow mask at a rate of 0.5Å /s. Rubrene (Aldrich) is then thermally evaporated onto the substrate at 1×10^{-7} Torr after being purified by the temperature gradient sublimation approach.[36] In addition to the standard cleaning procedure with DI-water, acetone, trichloroethylene and 2-propanol, 20 minutes of UV ozone treatment was applied to increase the surface energy. The deposition rate of the rubrene is in the range of 0.1Å /s to 0.3Å /s and the film thickness is 60nm. The sample is then annealed at 80°C in vacuum for 15hrs to obtain good crystallinity of the rubrene film. The channel length (L) and width (W) defined by the shadow mask are 50μm and 350μm respectively.

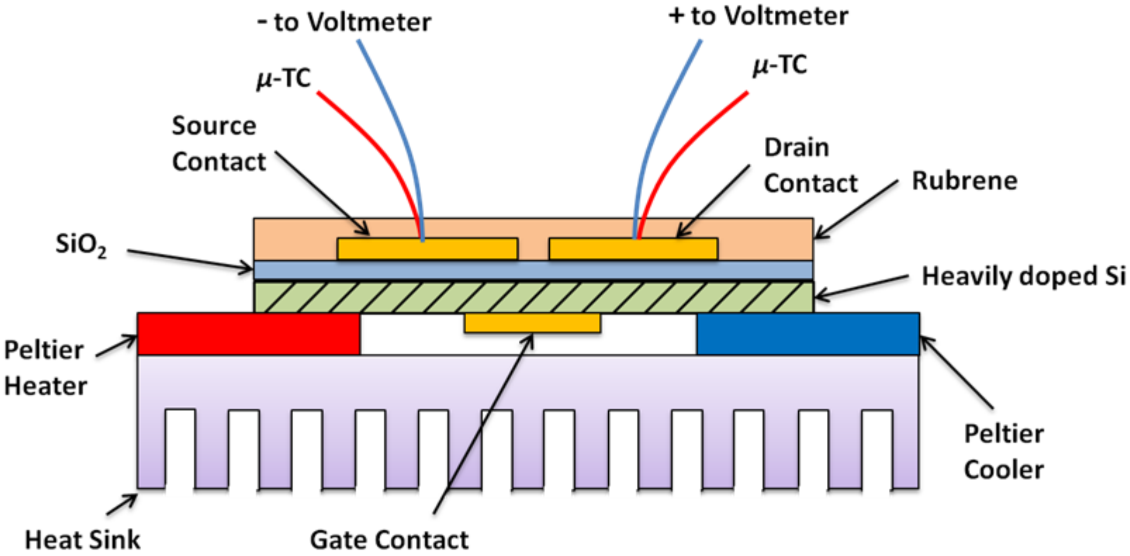

Figure 11 Schematic diagram of the bottom contact rubrene OTFT device structure and the setup for Seebeck measurement.

The fabrication of pentacene top contact OTFTs follows similar procedures as the rubrene bottom contact OTFTs. However, there are still some differences in terms of deposition sequence, self-assembly-monolayer (SAM), etc. An SAM layer of

Octadecyltrichlorosilane (OTS) is applied on the thoroughly cleaned and UV treated dielectric surface by immersing the samples into a bottle containing diluted OTS solution. The solvent used is trichloroethylene, and the bottle is sealed after nitrogen is filled into it for the purpose of lowering water concentration. The sample is taken out 24hrs after its exposure to the OTS solution, and then rinsed with trichloroethylene. In the thick sample (50nm), the OTS treated samples are immediately placed into the evaporation chamber for pentacene deposition, and 60nm thick Ag electrodes are then deposited onto the 50nm thick pentacene. The channel length is 150μm and the channel width is 1150μm. In the thin sample (10nm), the electrodes are still 60nm but the channel length and width is changed to 204μm and 3500μm to obtain larger drain-source current. The reason for using large W/L ratio in the thin sample is that the thin pentacene layer tends to yield small channel current due to discontinuous film formation. A large W/L ratio helps reduce the reading error in the measurements and can be normalized into the final calculations.

2.4.3 Thermoelectric Measurement

For the Seebeck coefficient measurement, the OTFTs are placed on a testing stage with two thermoelectric modules, one of which is the cooler and the other serves as the heater. A linear temperature gradient is achieved across the channel in the OTFT, and the temperature difference (ΔT) across the drain source electrodes is measured by the type-T micro-thermocouple (μ-TC) on the rubrene surface (Figure 11)).The Seebeck coefficient of the rubrene OTFT is calculated by $S = \frac{\Delta V}{\Delta T}$.

In order to accurately evaluate the temperature differences between the OTFT channels, temperature linearity tests are conducted on each sample. Figure 13 shows one example of the test, conducted on a bottom contact rubrene OTFT sample. The temperature difference is fitted with a linear, which is then used to extrapolate the actual temperature difference across the channel. In the rubrene OTFT samples, the channel length is 50μm. Therefore, the measured temperature differences across the two thermocouples are extrapolated to 50μm. In Figure 12(b), the temperature differences are approximately 9^{o}C, but they are measured across a distance of 2mm. So the actual temperature differences across the channel, which give rise to the voltages in Figure 12(a), are approximately 0.23^{o}C. This technique has been used extensively in the study to evaluate the actual temperature differences across the channel, because in most cases the channels are too small for the thermocouples to be precisely placed.

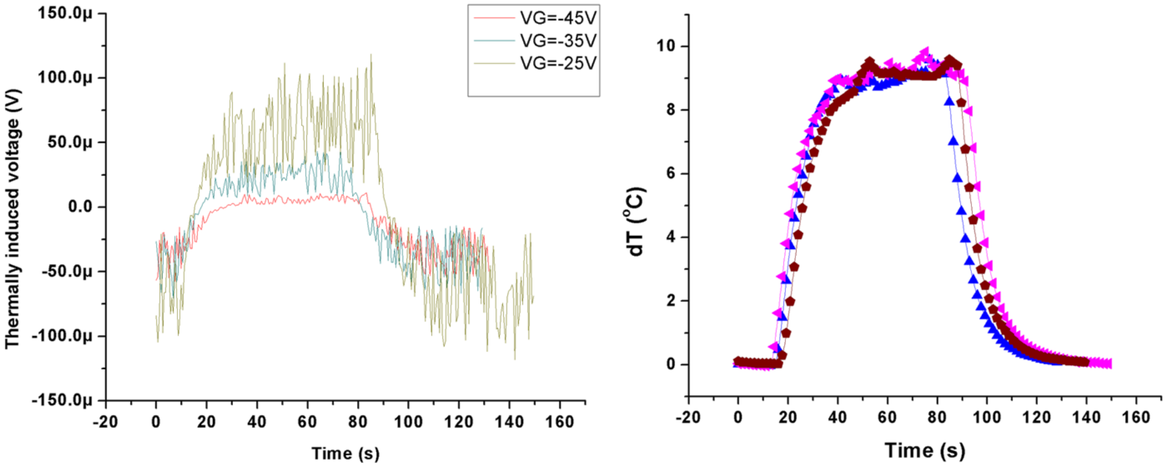

Figure 12 a) The thermally induced voltage on the rubrene OTFT at different gate biases. b) The temperature difference between the two micro-thermocouples with gate biases corresponding to those in a). The noise in the thermally induced voltage increases dramatically with the decrease of gate voltage, i.e. the decrease of $|V_G\text{-}V_{TH}|$, and the magnitude also increases correspondingly.

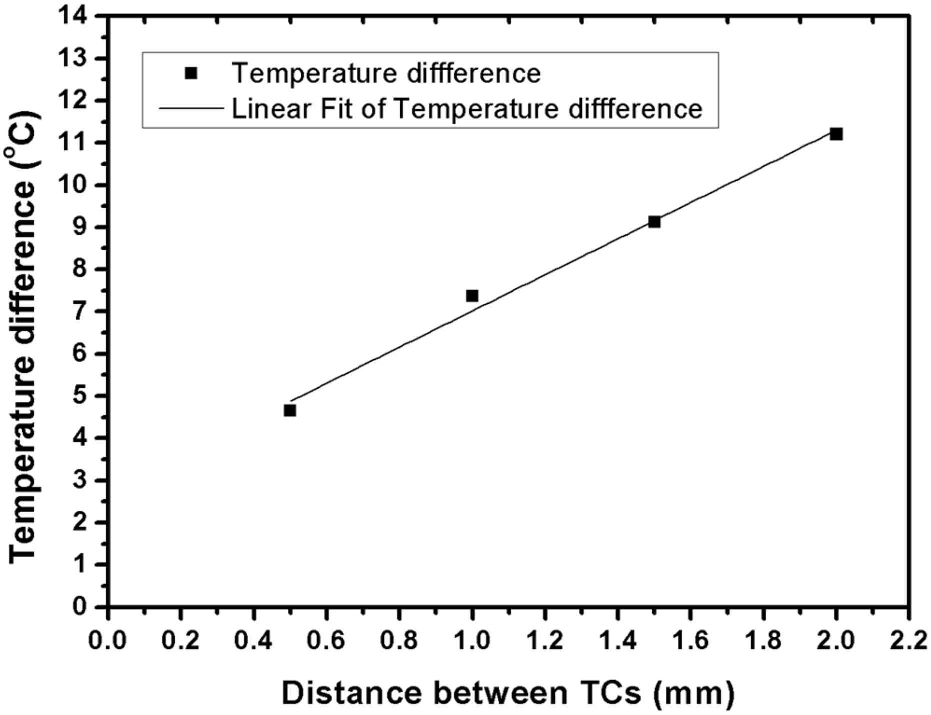

Figure 13 The fitting of the temperature difference – channel length relationship for the extrapolation of the temperature difference across the channel. The x-axis in this figure is the distance between the two thermocouples.

2.5 Effective channel thicknesses on bottom/top contact OTFTs

Under Maxwell-Boltzmann approximation, the volumetric carrier density (p') of the organic semiconductor is related to the Seebeck coefficient by, [37,38]

$$p' = N_m e^{-\frac{qS}{k}} \qquad \mathbf{8}$$

where N_m is the effective density of states (DOS), q is the electronic charge and k is the Botzmann constant. The value of N_m depends strongly on the nature of the semiconductor materials; for the thin film OTFT devices fabricated by ZnPc doped with F4 – TCNQ, the carrier density is close to the molecular density of the ZnPc. It is usually assumed that the effective density of states equals the molecular density of the organic semiconductor. This corresponds to the case in which each molecule contributes to one state.[18,19] Similarly, for the rubrene single crystal transistor, Pernstich *et al.* have shown that N_m of 2.85×10^{21} cm^{-3} corresponds to two states per rubrene molecule. The decrease of the Seebeck coefficient of the transistor attributes to the increase of the volumetric carrier density. Figure 15 shows the variation of the Seebeck coefficient as a function of gate bias of the rubrene OTFT under test. It can be clearly observed that when the magnitude of the V_G increases, the Seebeck coefficient drops according to the increase of the volumetric carrier density in the channel.

Before evaluating the field-effect-modulated Seebeck coefficient on the device, it is necessary to evaluate the electrical properties of the transistor device, as the threshold voltage is of great importance to the operation of the OTFT. Charge accumulation occurs after the gate voltage exceeds the threshold voltage. Figure 14 (a) and Figure 14 (b) shows the output and the transfer characteristics of the rubrene OTFT, from which the threshold voltage is extracted. The threshold voltage of the device is used to evaluate the areal carrier density in the transistor channel, which is given by,[11]

$$p = \frac{C_i\left(V_G - V_{th}\right)}{q} \qquad \mathbf{9}$$

where C_i is the capacitance of the insulating dielectric per unit area, V_{th} is the threshold voltage, and q is the electron charge. Hence, by comparing the volumetric and areal carrier density obtained by Eq. (2) and Eq. (3), the channel thickness of the organic transistor can be evaluated.

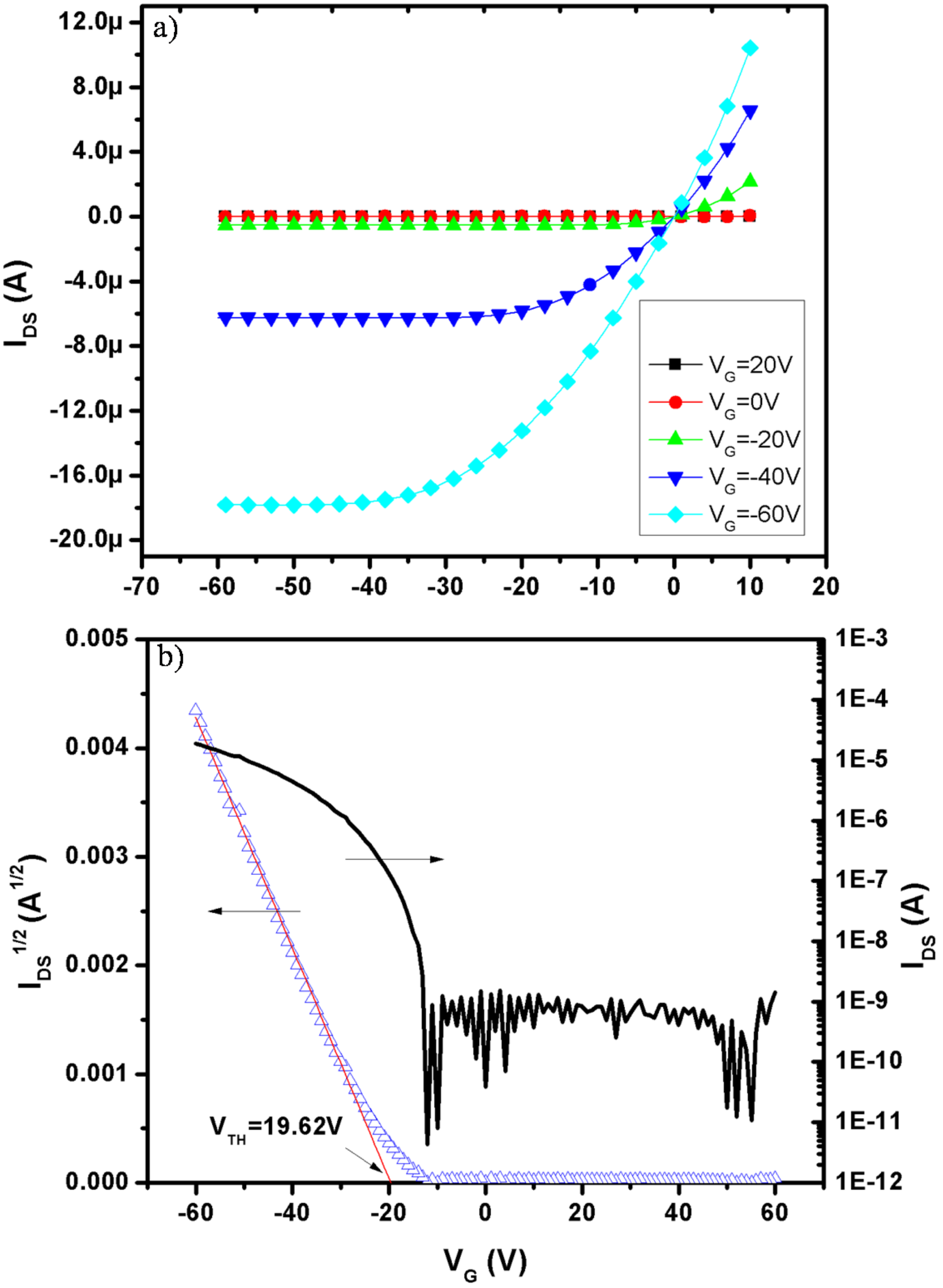

Figure 14 The output (a) and transfer (b) characteristic curves of the rubrene thin film OTFT. The threshold voltage obtained from (b) is -19.2V

The Seebeck coefficient of the rubrene OTFT can be modulated by field effect supplied through the bottom contact transistor structure, as shown in Figure 15. Generally the Seebeck coefficient drops when $|V_G|$ increases. This is reasonably correlated with the inter-dependency between the Seebeck coefficient and the electrical conductivity, which is proportional to the carrier concentration within the channel. Figure 16 shows the channel thickness as a function of gate bias. A significant increase of channel thickness can be observed as the gate bias decreases until the thickness clamped at around 1.3nm when $|V_G-V_{th}| > 10V$. This finding suggests that at low $|V_G-V_{th}|$ bias, the induced charges are spreading out to a relatively thick region of rubrene thermally evaporated on top of the silicon dioxide dielectric material.

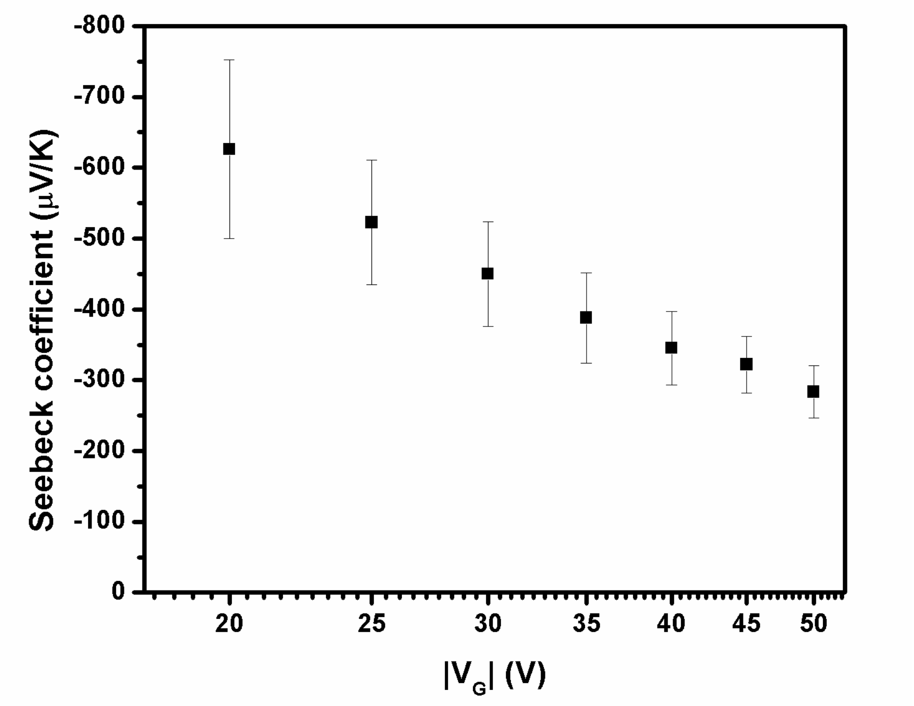

Figure 15 The measured Seebeck coefficient of the OTFT as a function of gate bias. At low gate bias, the relatively large deviation is related to the significant decrease in the conductivity of the rubrene thin film at low bias.

Alternatively, when the OTFT is under large gate bias, the charges accumulate to the first monolayer of the rubrene deposited on top of the dielectric. These experimentally measured channel thicknesses are further compared with the theoretical values obtained by the Debye length under different gate bias. The Debye length (L_D) has a dimension of length which can be consider as the effective channel thickness of the charge accumulation layer. It is given by, [39]

$$L_D = \frac{2\varepsilon_s kT}{qC_i(V_G - V_{th})} \qquad \mathbf{10}$$

and ε_s is the permittivity of the semiconductor ($\varepsilon_s = 2.6\ \varepsilon_0$ for rubrene). The Debye length shows a comparable channel thickness to the experimental results obtained by the thermoelectric measurements as shown in Figure 16, but the deviation becomes larger as the gate bias approaches to two extremes. The reason for this discrepancy needs to be explained in two regimes. At low $|V_G\text{-}V_{th}|$ regime, as can be seen in Eq. (4), the Debye length approaches to infinity and the measured thermoelectric effect is mainly contributed by the intrinsic carriers in the organic semiconductor. The deviation between the measured channel thickness and L_D at low gate bias is possibly due to the unintentional doping effect from the oxygen during the measurement under ambient condition. [40] On the other hand, at large gate bias, the calculated Debye length continuously decreases while our measurements show the measured channel thickness would be clamped at 1.3nm. The reason for this clamping can be attributed to the physical nature of the layer by layer deposition mode of the organic semiconductors. Unlike inorganic semiconductors that are held together by the covalent bonds, organic semiconductors are deposited onto the substrate in layer form and held together by Van der Waals force. So the charges induced by the gate bias in OTFT would accumulate in step form, rather than continuous form typical for inorganic semiconductors. In our experiment, the channel thicknesses are 1.36nm, 1.22nm, 1.31nm and 1.20nm at $|V_G-V_{th}|$ = 15V, 20V, 25V and 30V, respectively. These values are in the proximity of the height of one rubrene monolayer (ML height = 1.3nm)[41], indicating a restriction in dimension for the carrier concentration.

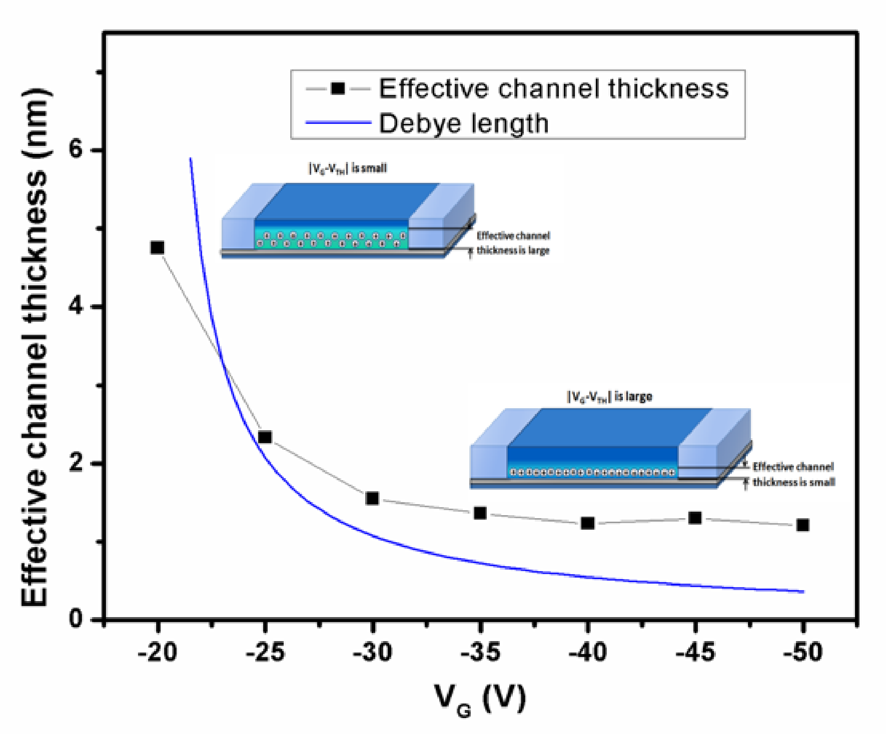

Figure 16 Effective channel thickness as a function of V_G and its comparison with the Debye length. It can be observed that the channel thickness clamps when V_G keeps increasing in magnitude. V_{th} is -19.6V, and large $|V_G|$ corresponds to narrower channel, and smaller $|V_G|$ wider channel.

Since the bottom contact OTFTs does not have the capability to rule out the discontinuous formation of organic materials near the metal electrodes, top contact

OTFTs are introduced as a comparison as well as confirmation of the abovementioned method of deriving the effective channel thickness. In addition, pentacene is used in the top contact OTFTs because of its superiority in terms of mobility. Despite large pentacene single crystal transistors cannot be easily fabricated, pentacene thin film transistor is simple to fabricate and constantly yields better electric properties than most of the other small molecular weight organic materials, including rubrene thin film. The only issue that prevents effective bottom contact pentacene OTFT fabrication is its necessity to apply an SAM layer (OTS), whose application method is not compatible with metal electrodes. The electrical properties of the pentacene OTFT with 50nm thick pentacene film is shown in Figure 17, with Figure 17 (a) showing the output characteristic and Figure 17 (c) showing the transfer characteristic. The electrical properties of the 5nm thick pentacene OTFT for validating the effective channel thickness clamping effect is also shown in Figure 17 (b) and Figure 17(d). There are three points of interests in terms of electrical characteristics. Firstly, the mobility of the 50nm thick pentacene OTFT is 0.025cm^2/V·s, more than twice larger than the 0.011cm^2/V·s obtained on the 5nm thick pentacene OTFT fabricated under same conditions. It is conformal the previous observation for thickness dependent mobility on pentacene OTFT in Ref. 42 . The discontinuous pentacene film formation within the channel drags down the channel conduction and thus the field effect mobility. Secondly, the depletion current of the 5nm device is about one order of magnitude larger than the 50nm sample. This is probably caused by the oxygen doping effect that affect the thinner films more than the thicker films, because the thinner films have relatively loose molecule arrangement and are more susceptible to oxygen diffusion. Thirdly, the threshold voltage is shifted about 3V toward the positive side. This could be associated with the same oxygen doping effect as oxygen diffusion into the thinner film causes more hole traps near the organic-dielectric interface. Therefore, it absorbs more induced hole charges when the gate biases are applied. On the other hand, at large gate bias, the calculated Debye length continuously decreases while our measurements show the measured channel thickness would be clamped at around 1.3nm for the rubrene OTFT and 1.2nm for the pentacene OTFT.

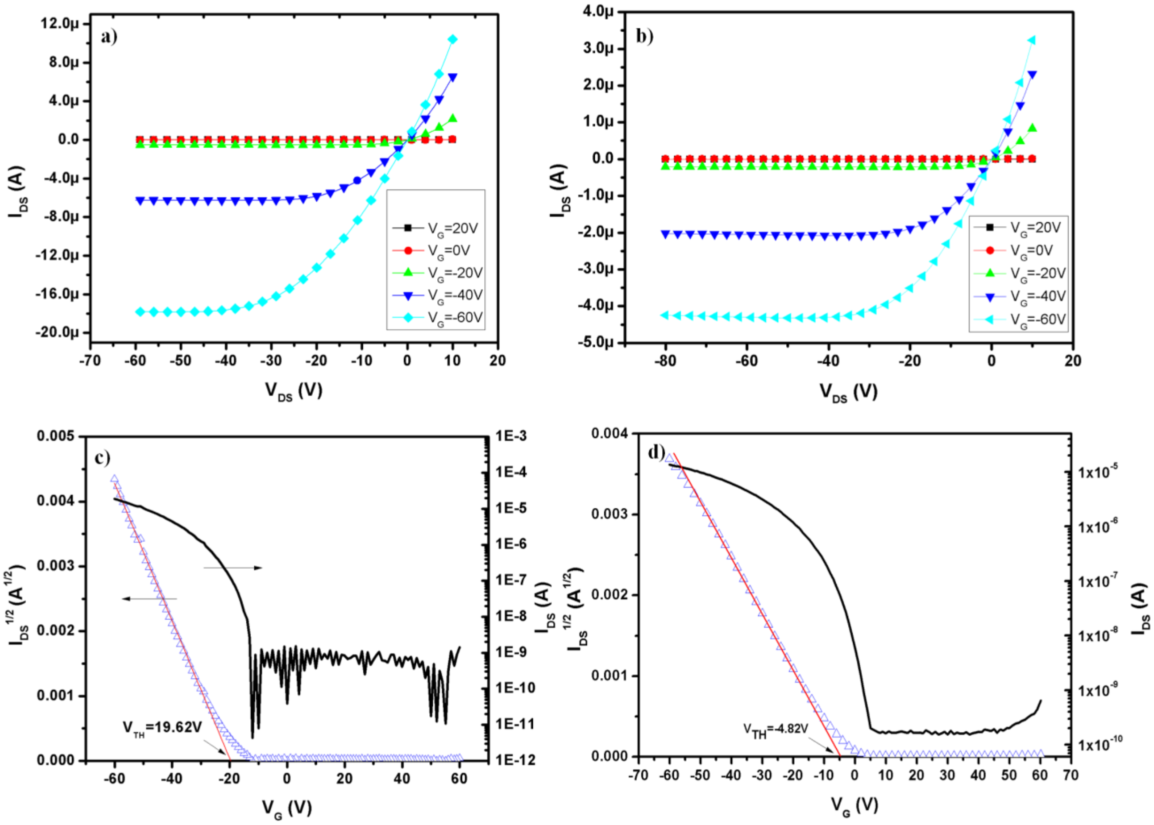

Figure 17 The output (a) and transfer (c) characteristics of the bottom contact rubrene thin film OTFT, and the output (b) and transfer (d) characteristics of the top contact pentacene thin film OTFT. The threshold voltage is -19.2V for the rubrene OTFT and -4.8V for the pentacene OTFT.

In our experiment, the channel thicknesses of the rubrene OTFT are 1.36nm, 1.22nm, 1.31nm and 1.20nm at $|V_G\text{-}V_{th}|$ = 15V, 20V, 25V and 30V, and those of the pentacene OTFT are 1.29nm, 1.05nm and 1.19nm at $|V_G\text{-}V_{th}|$ = 20V, 25V and 30V.(Figure 19) These values are in the proximity of the height of one rubrene monolayer (ML height = 1.3nm)[43], and one pentacene monolayer (ML height = 1.5nm)[44], indicating a restriction in the dimension for the carrier concentration.

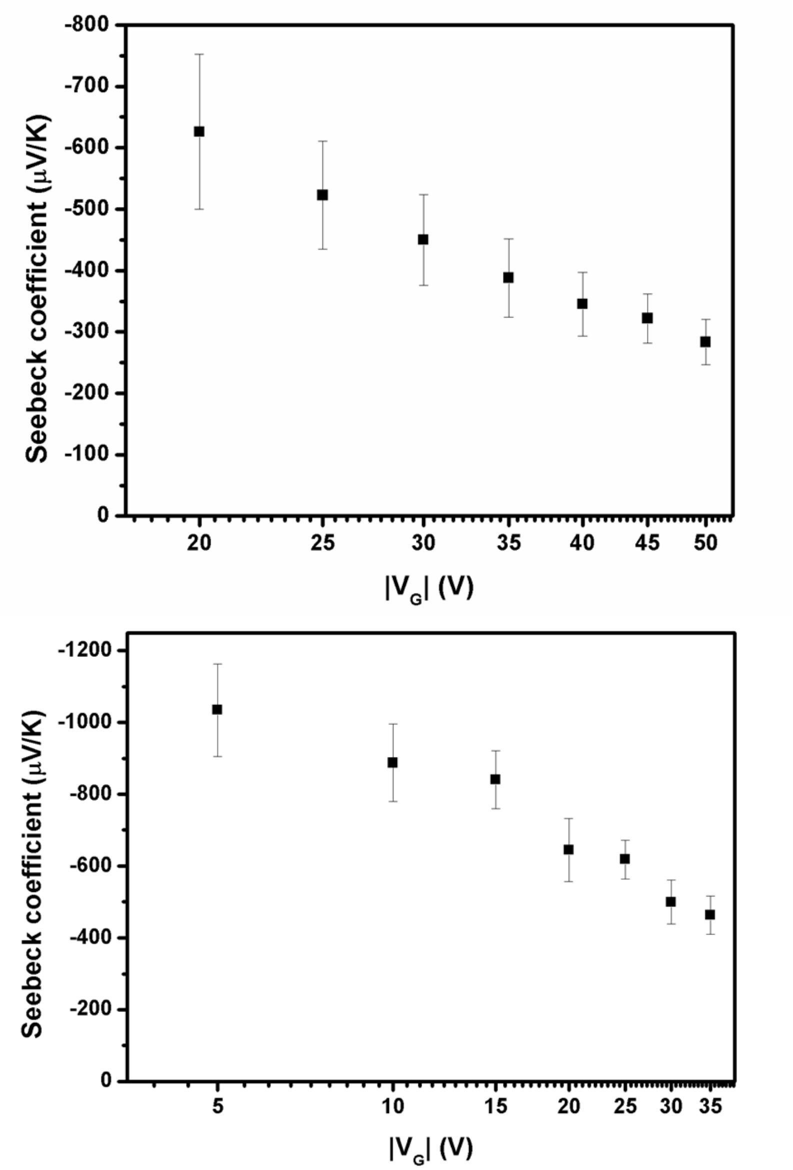

Figure 18 The measured Seebeck coefficient of the rubrene OTFT (a) and pentacene OTFT (b) as a function of gate bias. At low gate bias, the relatively large deviation is related to the significant decrease in the conductivity of the rubrene thin film at low bias.

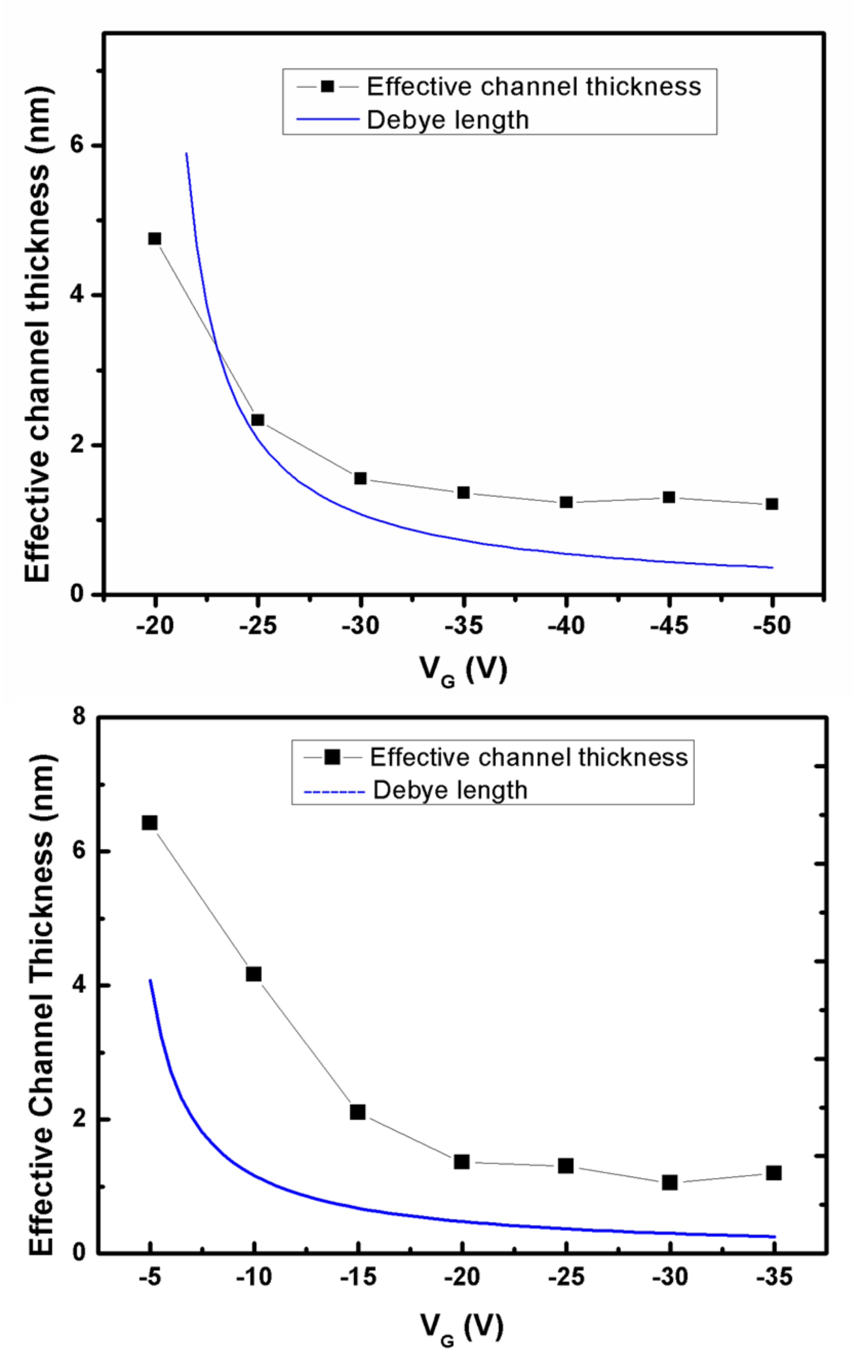

Figure 19 The measured effective channel thickness of the rubrene OTFT (a) and the pentacene OTFT (b) as a function of |VG-Vth| and their comparison with the Debye length. It can be observed that the channel thickness clamps when |VG-Vth| keeps increasing.

2.6 Conclusions

To summarize, we have demonstrated that, by evaluating the volumetric carrier density in the carrier accumulation channel in rubrene bottom contact and pentacene top contact OTFTs from the Seebeck coefficient, the effective channel thickness can be evaluated as a function of applied gate voltage. In our rubrene OTFT, the channel thickness decreases as much as 67%, from around 4.75nm to 1.55nm, when $|V_G-V_{th}|$ increases from 0.4V to 10V and clamps at about 1.3nm as $|V_G-V_{th}|$ keeps increasing, indicating a concentration of carriers with its dimension limited by the monolayer height. In our pentacene top contact OTFT for the comparison, the effective channel thickness also changes, from 6.42nm to 1.36nm as $|V_G-V_{th}|$ varies from 0.2V to 15V. The effective channel thickness obtained by this method has taken into account the collective contributions from both the complete film and the islands on the top, and is useful in determining the optimal contact structure and height in bottom contact OTFTs with different ranges of operating gate voltages. Its validity in bottom contact OTFTs are confirmed by the similar results in the top contact pentacene device.

Overall, the thermoelectric characterization technique employed in the current work provides a generic non-destructive technique for the quantitative characterization of the effective channel thickness in OTFT with virtually no extra sample preparation procedures, facilitating the characterization of carrier transport properties in various types of OTFT devices in their final forms.

3 Enhancement of Seebeck coefficient for Anodized Titanium Oxide Nanotube Array and Organic Semiconductor

3.1 Enhancement of Thermoelectric Figure-of-Merit of Titanium Oxide by Nanostructure

3.1.1 Thermoelectric effect on titanium oxides

Titanium Oxide (TiO_x) is an attractive inorganic semiconductor material because of its wide applications, including solar cells, pigmentation and photocatalyst, and had been intensively studied in terms of electrical and optical properties.[45] Only recently have the thermoelectric properties of TiO_x become a point of interest. In fact, in a larger scope, the thermoelectric property of metal oxides, including TiO_x, has already attracted much attention since the middle of the 1990s. Various metal oxides, such as Na_xCoO_4, $Ba_{1-x}Sr_xPbO_3$, and $(ZnO)_m In_2O_3$, have been found to exhibit high thermo-electromotive force,[46] and new theoretical approaches have been developed to derive thermoelectric properties in strongly correlated electron systems.[47] From the practical point of view, thermoelectric materials consisting of non-hazardous and inexpensive elements are highly desirable.[48] Therefore, TiO_x becomes one of the most promising candidates for these applications, both in anatase and rutile phases, two predominant crystalline phases of titanium oxides.

However, TiO_x, also denoted as Ti_nO_{2n-1} (n is an integer greater than 2), can have various compositions of Ti and O and thus exhibit different thermoelectric properties when they are fabricated under different conditions. For example, Okinaka *et al* have demonstrated that $TiO_{1.1}$ has a thermoelectric figure-of-merit (ZT) as high as 1.64 (p type).[49] This is achieved at around 800°C, as shown in Figure 20, and is considered high enough to make TiO_x commercially attractive for various thermoelectric applications near that temperature range.

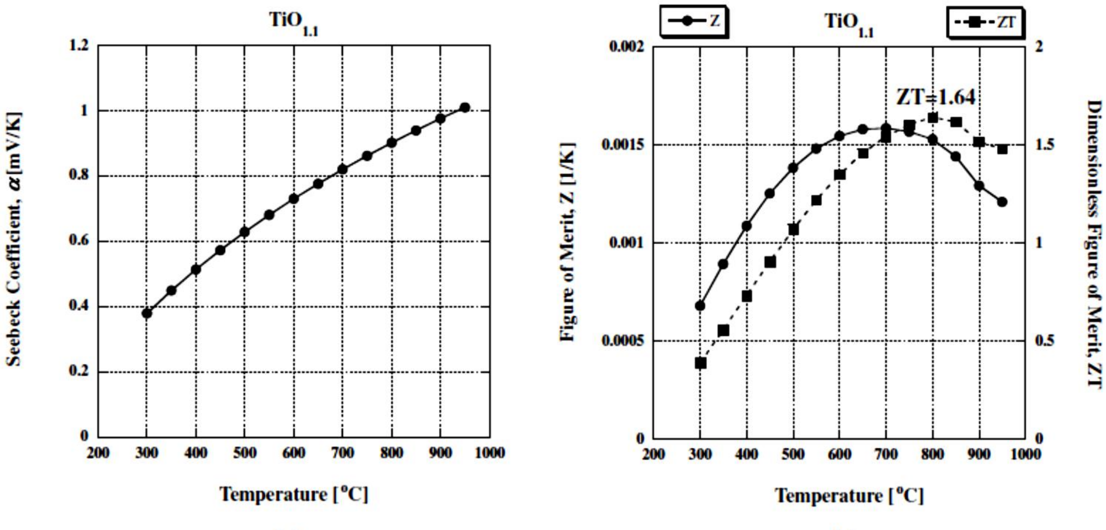

(a) (b)

Figure 20 Thermoelectric properties of $TiO_{1.1}$ with regard to temperature. a) Seebeck coefficient. b) Figure of merit Z and dimensionless figure of merit ZT. At around 800°C the undoped nonstoichiometric titanium oxide achieved a highest ZT of 1.64.

(Source: N. Okinaka and T. Akiyama, *Jpn. J. Appl. Phys.*, **45**, 7009 (2006))

Unlike Okinaka *et al*'s efforts, in a separate series of studies, He *et al*. have measured Seebeck coefficients on bulk titanium oxide pellets fabricated by hot press method.[50] The pellets formed at different oxidization temperatures showed naturally varying oxygen contents and Seebeck coefficients. The bulk $TiO_{1.83}$ pellets had a ZT up to 0.23 at 800°C. This value is substantially smaller than what Okinaka *et al* obtained, but can still be considered a high value for potential applications in thermoelectric power generation.

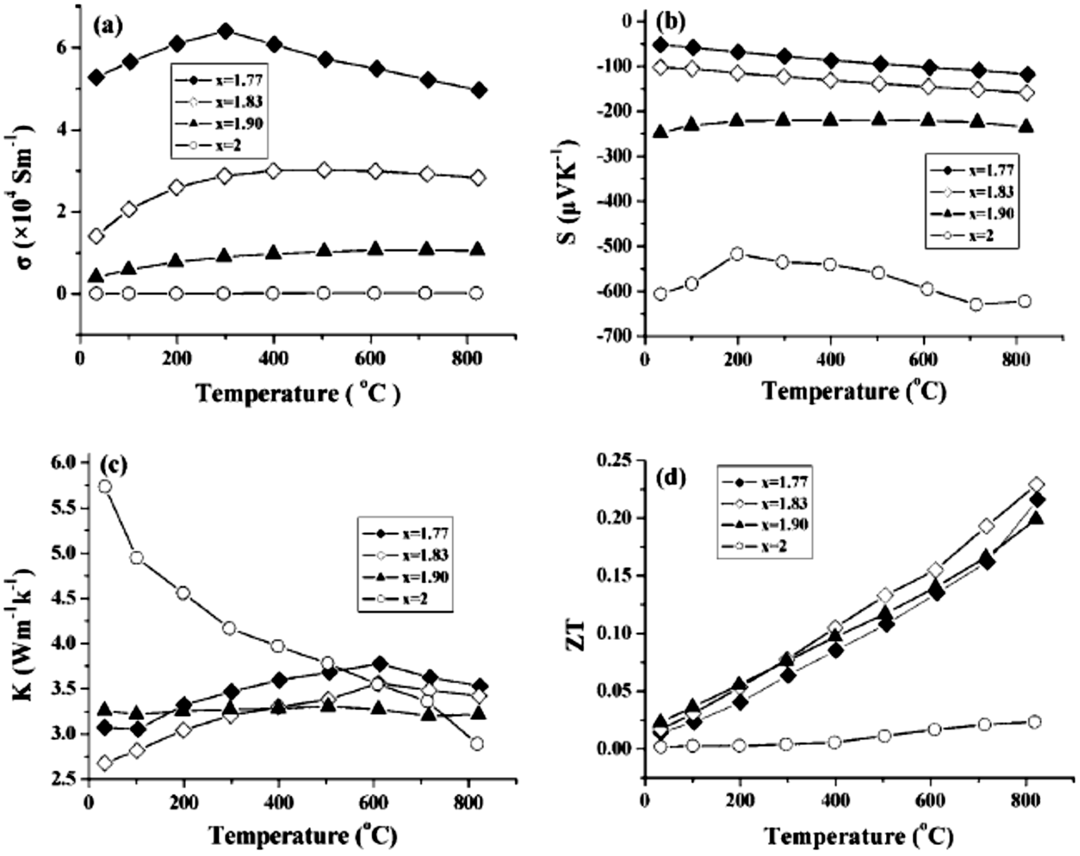

Figure 21 a) Electrical conductivity as a function of temperature, b) Seebeck coefficient, c) thermal conductivity and d) thermoelectric figure of merit of TiO_x with x=1.77, 1.83, 1.90 and 2.

(Source: Q. He, Q, Hao, G. Chen, B. Poudel, X. Wang, D. Wang, Z. Ren, *Appl. Phys. Lett.* 91, 052505, (2007))

3.1.2 Sign change of Seebeck coefficient by oxygen composition and doping

In the thermoelectric study of nonstoichiometric titanium oxides, besides obtaining highest thermoelectric properties, it is also important to know the behavior and the mechanism of the dependence of thermoelectric properties on different TiO_x compositions. In He *et al*'s experiments, aside from the high Seebeck coefficient and figure of merit, a change of conduction type was also observed and investigated in detailed comparison of TiO_x with different oxygen compositions. Figure 22 (a) shows the room temperature Seebeck coefficient as a function of x value in TiO_x. The Seebeck coefficients are found to be negative for x = 1 to 1.25, indicating electrons are the dominant charge carrier. This is not in agreement with the observations of Okinaka *et al*, in which positive Seebeck coefficients are measured. Furthermore, for x = 1.25 to 5/3, the holes becomes dominant, and then for x = 5/3 to 2, electrons is again the major charge carriers inside the material. On the other hand, even for samples with a fixed x, the conduction type also changes, either from p-type to n-type or from n-type to p-type. This was exemplified by Figure 22 (b), in which two TiO_x samples with x = 1.07 and 1.46 showed exactly opposite direction of conduction type conversion, with $TiO_{1.07}$ changing from p-type to n-type when temperature increases over a threshold temperature at around 500^oC and $TiO_{1.46}$ changing from n-type to p-type when temperature decreases below a threshold temperature at around 500^oC.

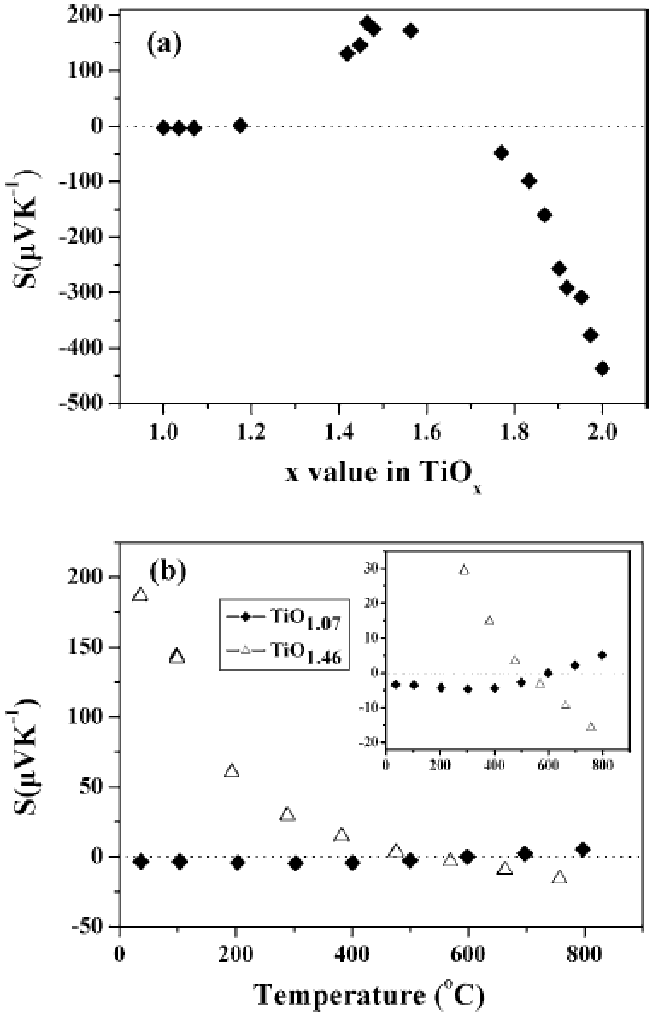

Figure 22 a) Seebeck coefficient at room temperature, b) Seebeck coefficient as a function of temperature for $TiO_{1.07}$ and $TiO_{1.46}$. The inset is an enlarged view of the region where two curves crosses the 0 value for S.

(Source: Q. He, Q, Hao, G. Chen, B. Poudel, X. Wang, D. Wang, Z. Ren, *Appl. Phys. Lett.* 91, 052505, (2007))

Besides varying the oxygen composition, doping is also an effective measure to increase thermoelectric ZT for TiO_X. By varying the dopant material and concentration, Nowotny *et al* had characterized the effect of oxygen activity on the charge transport properties of niobium-doped titanium dioxide by thermoelectric measurements.[51] In their work, TiOx were doped to show Seebeck coefficients (S) varying from -750uV/K (n-type) to 107uV/K (p-type). Not only does TiO_x exhibit high S, they also exhibit a change of sign with different doping levels. According to their experiments, undoped titanium oxide in anatase phase had a normally negative Seebeck coefficient, while 1at. % doping of Fe makes it positive. The 0.35at. % doping of Nb, however, obtained a negative Seebeck coefficient again. This was believed to be caused by the shift of the Fermi level, with the downward shift caused by Nb doping moving the Fermi level towards the lower limit of the conduction band, and the upward shift caused by Fe doping moving the Fermi level towards the upper limit of the valence band.

3.1.3 Enhancement of titanium oxides' thermoelectric properties by nanostructures

Despite some successful moves in tuning up the Seebeck coefficient and the thermoelectric figure of merit, the abovementioned enhancement of thermoelectric properties of TiO_x, as well as the sign change phenomenon of the Seebeck coefficient, are mostly conducted and realized in bulk scales. In order to drive the S and zT even higher, structural modifications is one of the potentially effective measures. Recent studies have found that low dimensional structures, or nanostructures, have great impact on the enhancement of thermoelectric properties on various material systems.[48-51] One of the two ideas behind the enhancement by nanostructure is the quantum-confinement that helps achieve high power factor, $S^2\sigma$. The reason for the importance of the quantum-confinement effect is that it introduces lengths as a parameter to allow the control of the Seebeck coefficient and the electrical conductivity independently. Researchers have found this effect as an effective way to maximize the power factor and optimizing the S-σ interdependency.[5657] The other idea is that through nanostructures, the thermal conductivity, κ, can be reduced in a greater degree than the electrical conductivity, σ. The reasoning behind this idea is that the two properties are affected by different scattering lengths.[58] Specifically speaking, the myriads of interfaces created by nanostructures can scatter phonons more effectively than electrons, and furthermore, scatter the phonons that contribute most to the thermal conductivity than those who do less. Figure 23 shows the electronic density of states as varied by the nanostructures, in which the quantum wire case Figure 23 (c) is an example of nanotube structure.

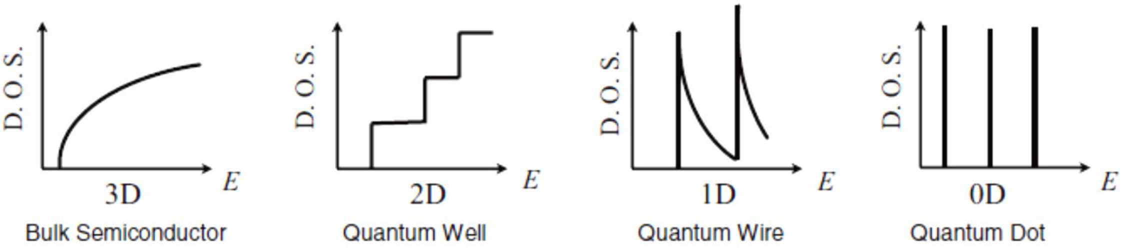

Figure 23 Electronic density of states for a) bulk 3D crystalline semiconductor, b) 2D quantum well, c) 1D nanowire or nanotube, and d) 0D quantum dot.

(Source: M. S. Dresselhaus, G. Chen, M. Y. Tang, R. Yang, H. Lee, D. Wang, Z. Ren, J. P. Fleurial, and P. Gogna, *Adv. Mater.*, **19,** 1043 (2007))

In this chapter, the enhancement of the thermoelectric properties by nanostructure is combined with the variation of the oxygen composition in the non-stoichiometric titanium oxide. TiO_x nanotubes are fabricated and thermally treated under different pressure and temperature conditions. The Seebeck coefficients are found to have been greatly altered with various treatment conditions and a change of conduction type is also observed for the nanotube structured titanium oxides.

3.2 Titanium oxide nanotubes fabrication and in-plane thermoelectric measurement

Titanium oxide nanotubes were prepared by potentiostatic anodization of titanium metal foil (99.6% purity, Strem Chemical) in 0.25 wt% ammonium fluoride (98% purity) dissolved in ethylene glycol, in the presence of 2 wt% water. The annealed samples without water tend to develop cracks on the surfaces, which damages the integrity of the nanotube arrays.[59,60] Prior to anodization, Ti metal foils (200 μm thick) were cleaned by ultrasonication in acetone, isopropanol and trichloroethylene, followed by rinsing with deionized water and dried by nitrogen gas. The anodization was performed in a two-electrode configuration as illustrated in Figure 24, with Ti foil as the anode and a platinum foil with identical shape as the cathode. A constant anode-to-cathode potential of 60V was supplied by a program-controlled DC source (N5751A, Agilent) for three hours. The nanotubes are grown on the Ti metal anode during this period, with its dimension and morphological properties determined by the voltage and the speed by which the voltage is raised, as well as the ammonium fluoride concentration in the solution. After the fabrication of TiO_2 nanotubes, the samples were cleaned in a sonication bath for 50s in de-ionized water with 0.8 wt% of Al_2O_3 nanoparticles of 300 nm diameter. This sonication step is utilized specifically to remove the surface debris covering the nanotube array, as shown in Figure 25 (a). The effect of the removal is conspicuous, as the surface debris is seen completely removed by the sonication in Figure 25 (c). The 50s sonication totally removed 12.6μm thick surface layer, indicated by the distinction between cross-sectional views Figure 25 (b) and Figure 25 (d).

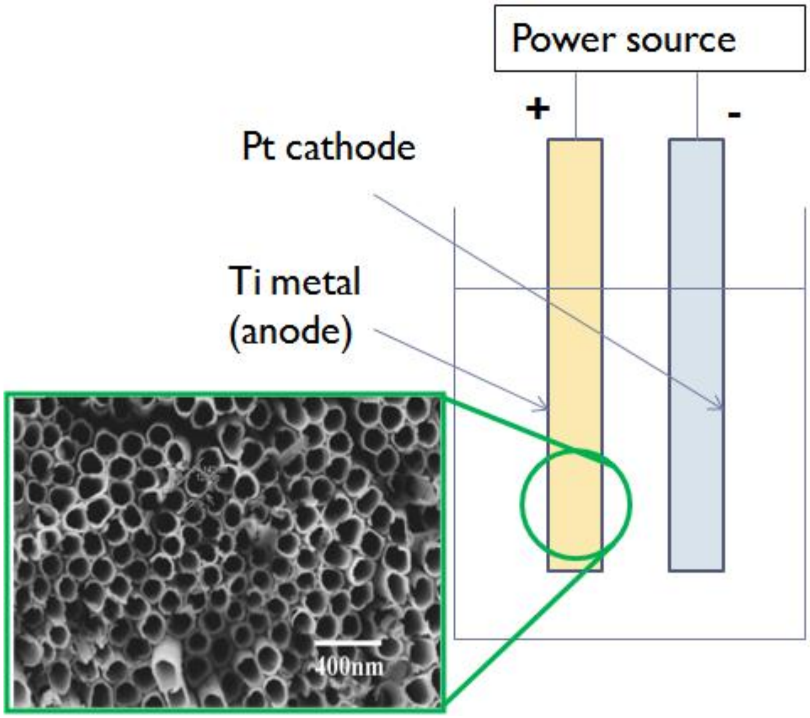

Figure 24 Schematic illustration of the potentiostatic anodization of titanium metal foil. The inset is the SEM image taken on one of the samples, illustratively showing that nanotubes are grown directly on the anode Ti metal foil in this setup.

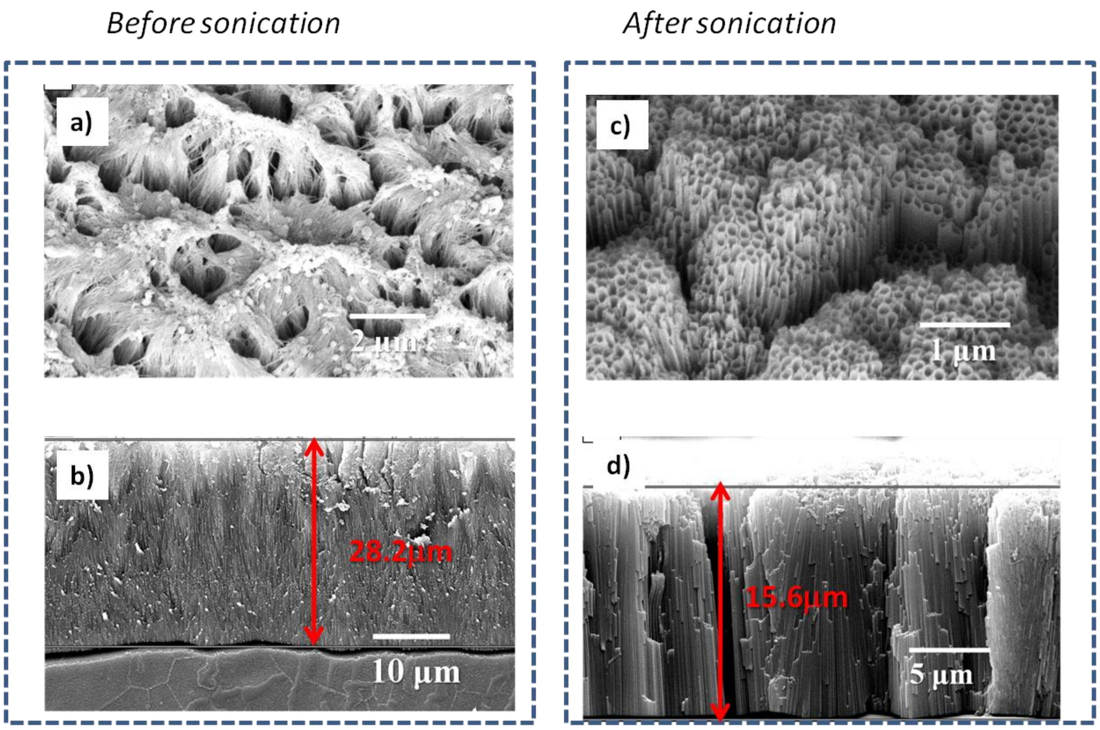

Figure 25 The surface debris covering the nanotubes underneath, shown in a) is removed by sonication and the surface morphology after sonication is shown in c). The total thickness of the titanium oxide layer is reduced from 28µm before the sonication to 15.6µm afterwards.

Besides the surface debris, the freshly prepared titanium oxide nanotubes has another morphological characteristics – surface roughness. A close look at the nanotubes as shown in Figure 26 reveals this characteristics explicitly. The roughness is caused by the fluctuation of the environmental temperature, as confirmed in Ref.[61]. This has essentially created more electron and phonon scattering sites by means of surface area maximization, and will show its effect in enhancing the thermoelectric properties in the next section of this chapter.

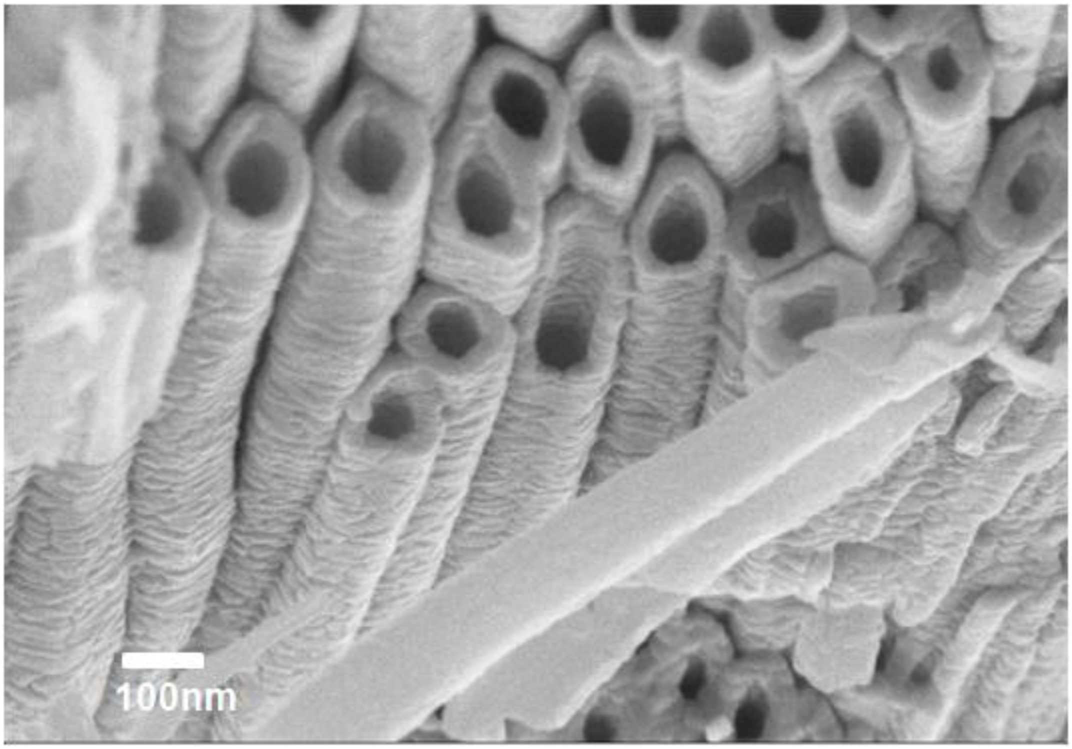

Figure 26 High magnification SEM image of the titanium oxide nanotube morphology. The roughness is caused mainly by the minute voltage fluctuation, while environmental factors such as temperature and flow pattern also have an impact.

Also worth mentioning as a morphological characteristic is the crack developing on the samples after the annealing processes. The cracks are macroscopic cracks that completely sever the conduction path across the nanotubes, so it is supposed to be prevented. In this chapter, a two-step annealing process is adopted to prevent the generation of thermal-stress-induced cracks.[13] In the first step, three of the six samples were annealed in air at 200^{o}C for two hours; in the second step, the annealing temperatures were raised to 450^{o}C, 525^{o}C and 600^{o}C, respectively, again in ambient environment. The other three samples underwent annealing processes with identical temperature profiles except that they were annealed in vacuum at a pressure of 5×10^{-5} Torr. After annealing, silver electrodes of thickness 100 nm were deposited on the nanotubes by thermal evaporation through a shadow mask with small holes of 1mm diameter and distanced at 6mm, at a base pressure of 7×10^{-7} Torr (E306, Edwards)

Thermoelectric measurements were performed by applying an in-plane temperature gradient along the samples, in which the temperature gradient was generated by two Peltier modules monitored by independent temperature controllers. The schematic diagram of the thermoelectric effect measurement setup is shown in Figure 27. The temperature difference across the Peliter modules was maintained at ~20^{o}C, and the cold side temperature was maintained above 15^{o}C to prevent water condensation on the samples which may affect the conductivity of the nanotubes.[62] For the voltage measurements, two 100-μm gold wires were connected to a digital multimeter (DMM) (34410A, Agilent) and the gold wires are assumed to have negligible effect on the thermoelectric voltage as measured. Temperature differences across the sample were measured by the micro-thermocouples with 30 μm diameter. The thermoelectric voltage and the temperatures were subsequently recorded for Seebeck coefficient evaluation.

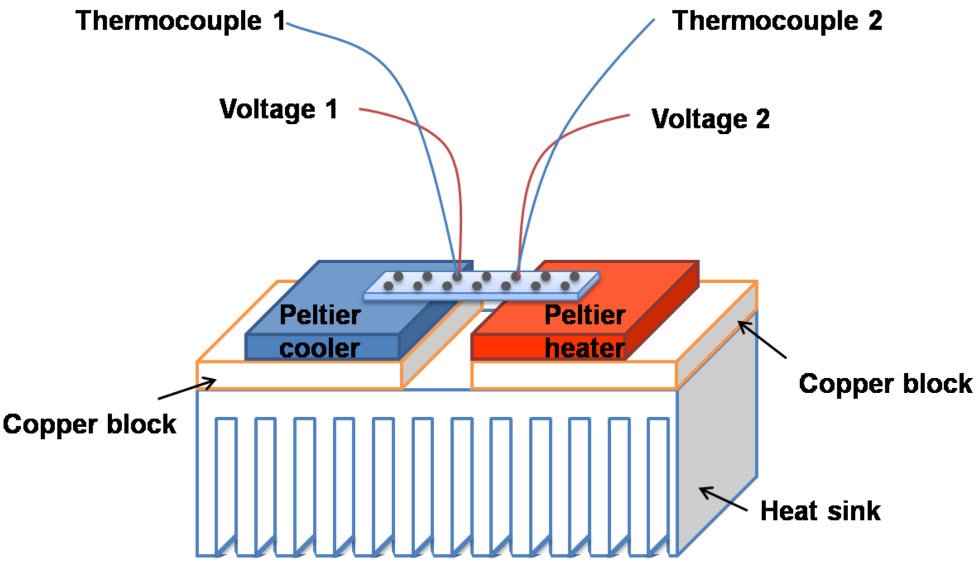

Figure 27 Schematic illustration of the setup for Seebeck measurement on TiOx nanotubes. The voltage signal and the temperature readings are transferred by the four micro-positioners with tungsten probes connected to gold wires of 100μm diameter. Silver dots of diameter 1mm are thermally deposited via a shadow mask with small dots spacing 6mm to each other (center-to-center).

3.3 Morphology and Seebeck coefficient of Nanotube TiOx

The Seebeck coefficients of the samples annealed under different conditions are listed in Table 1. Figure 28 plots the Seebeck coefficients of Samples A to F (conditions as shown in Table 1) as a function of average measurement temperature between the hot and cold side of the thermoelectric modules. As shown in the upper plot of Figure 28, Sample B annealed at 525^{o}C for five hours in ambient shows the largest Seebeck coefficient. This is an indication of the optimal temperature and duration for crystallization.[63] The magnitudes of the Seebeck coefficients increase with the averaged measurement temperature from -125.3μV/K at 25^{o}C to -292.6μV/K at 100^{o}C. This result agrees well with that obtained by He *et al*, where the bulk titanium oxide pellet showed a larger magnitude of the Seebeck coefficients while the temperature increased. The Seebeck coefficient also changes from -292.6 μV/K to 13.9 μV/K when the annealing is conducted at 525 °C but the atmosphere changes from air to vacuum (5×10^{-5} Torr). This finding agrees with the previous reports in Ref [24,25], where acceptor-highly doping turned TiO_2 into a p-type semiconductor.

Sample	**Sample configuration**	**Annealing condition**		**d_1/d_2**	**Seebeck coefficient at 25 $^\circ C$**	**Seebeck coefficient at 45 $^\circ C$**	**Seebeck coefficient at 70 $^\circ C$**	**Seebeck coefficient at 100 $^\circ C$**
		Temperature ($^\circ C$)	**Pressure (Torr)**					
A	Ti + nanotubes	450	760	0.786	-36.63	-38.97	-57.71	-99.91
B	Ti + nanotubes	525	760	0.809	-125.25	-117.1	-151.83	-292.55
C	Ti + nanotubes	600	760	0.853	-81.63	-128.98	-88.13	-168.8
D	Ti + nanotubes	450	5×10^{-5}	0.767	33.41	25.61	22.54	21.1
E	Ti + nanotubes	525	5×10^{-5}	0.831	19.82	16.7	17.86	13.9
F	Ti + nanotubes	600	5×10^{-5}	N/A	36.75	32.09	24.05	21.22
G	Ti foil only	No treatment	N/A	---	8.39	---	---	---
H	Ti foil only	525	760	---	9.91	---	---	---
I	To foil only	525	5×10^{-5}	---	9.15	---	---	---

Table 1 Treatment conditions, and Seebeck coefficients of the samples

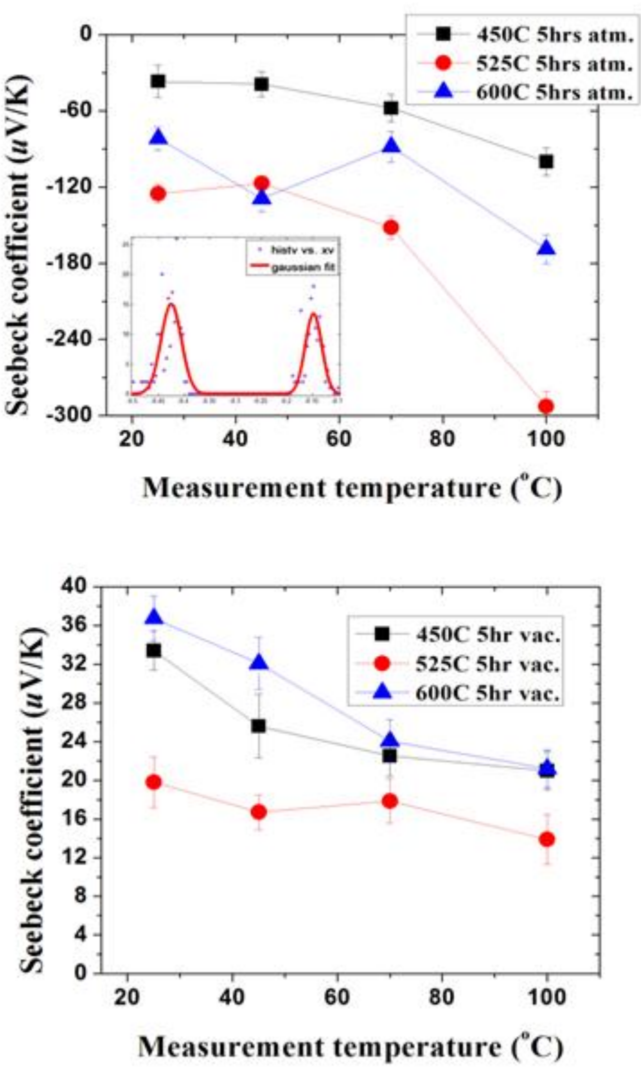

Figure 28 the Seebeck coefficients against the measurement temperatures for Samples A-F. The inset in the upper figure illustrates the way the Seebeck coefficients are calculated - the two Gaussian peaks correspond to the on- and off- states of the temperature difference.

Figure 30 shows the effect on the surface morphology of nanotube arrays by silver deposition. By comparing Figure 30 (a) and Figure 30 (b), it can be observed that from the top view, the silver contact is deposited on the sidewalls of the nanotubes and forms a continuous cover over the top surface. Figure 29 is another illustration of the sample, obtained by AFM imaging, in which TiOx nanotube array's top surface before sonication treatment and the one after sonication treatment are shown side by side. It is more than clear to reflect the total removal of the surface debris. On the other hand, in order to know whether the other side of the nanotube is also continuous, the bottom surface of the nanotubes that was peeled off from the titanium substrate is also shown in Fugure 29(c).

Figure 31 illustrates the effects of annealing conditions on the nanotube morphology. For Sample B annealed at 525^{o}C in air, the openings of the nanotubes are partially destroyed and some small crystals form on the edges, as shown in Figure 31 (a). If the annealing temperature is lowered to 425^{o}C, fewer crystals are found at the openings, as shown in Figure 31 (b). This agrees with the observation by Zhao *et al*., which stated that the destruction of the nanotubes was a result of the formation of rutile crystals.[68] If the sample is annealed at 600^{o}C in vacuum, the morphology of the nanotubes changes significantly, with their sidewalls deformed and the openings closed, as shown in Figure 31 (c).

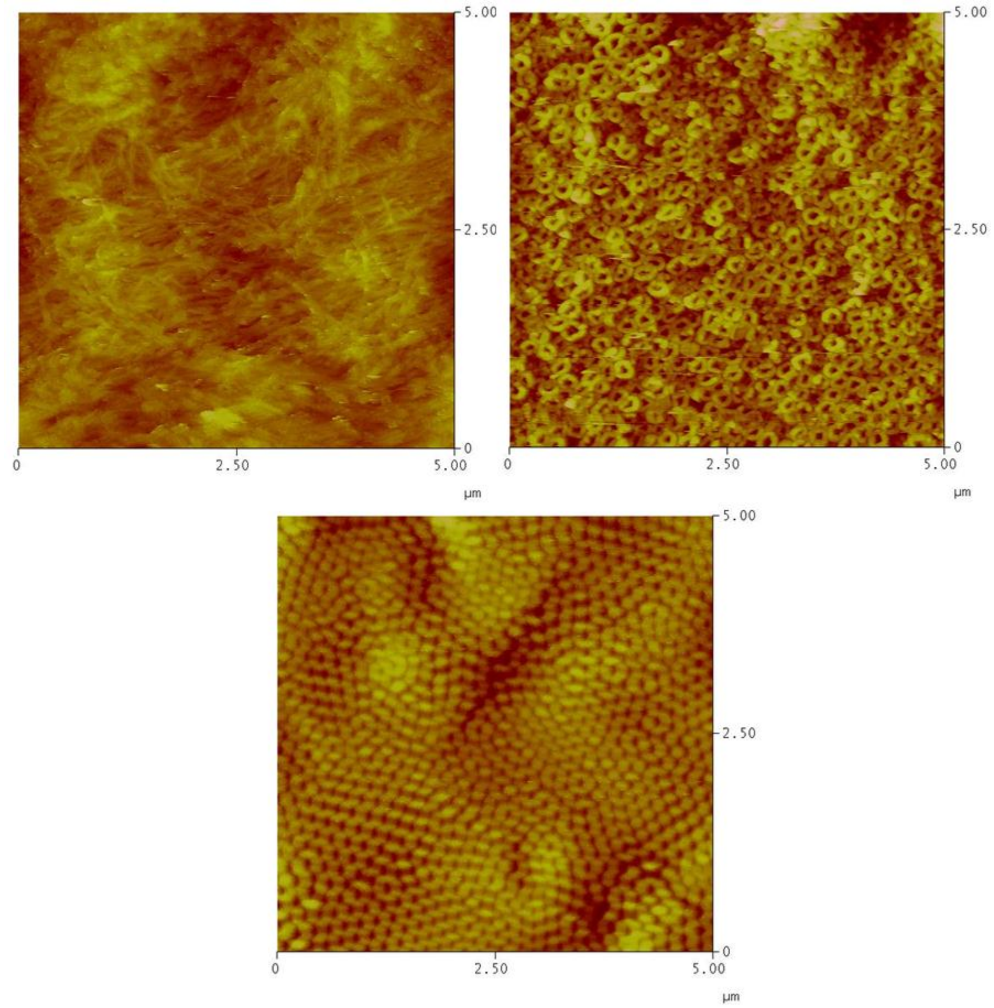

Figure 29 AFM images of the TiOx nanotube array's top surface a) before sonication treatment, and b) after sonication treatment. c) The bottom surface of the nanotubes that are peeled off from the titanium substrate.

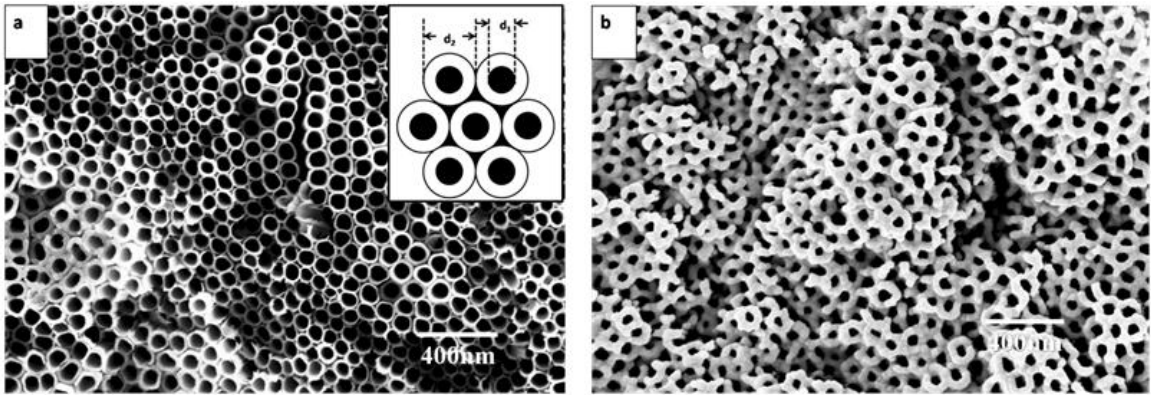

Figure 30 the SEM images of the nanotubes (a) before and (b) after silver deposition.

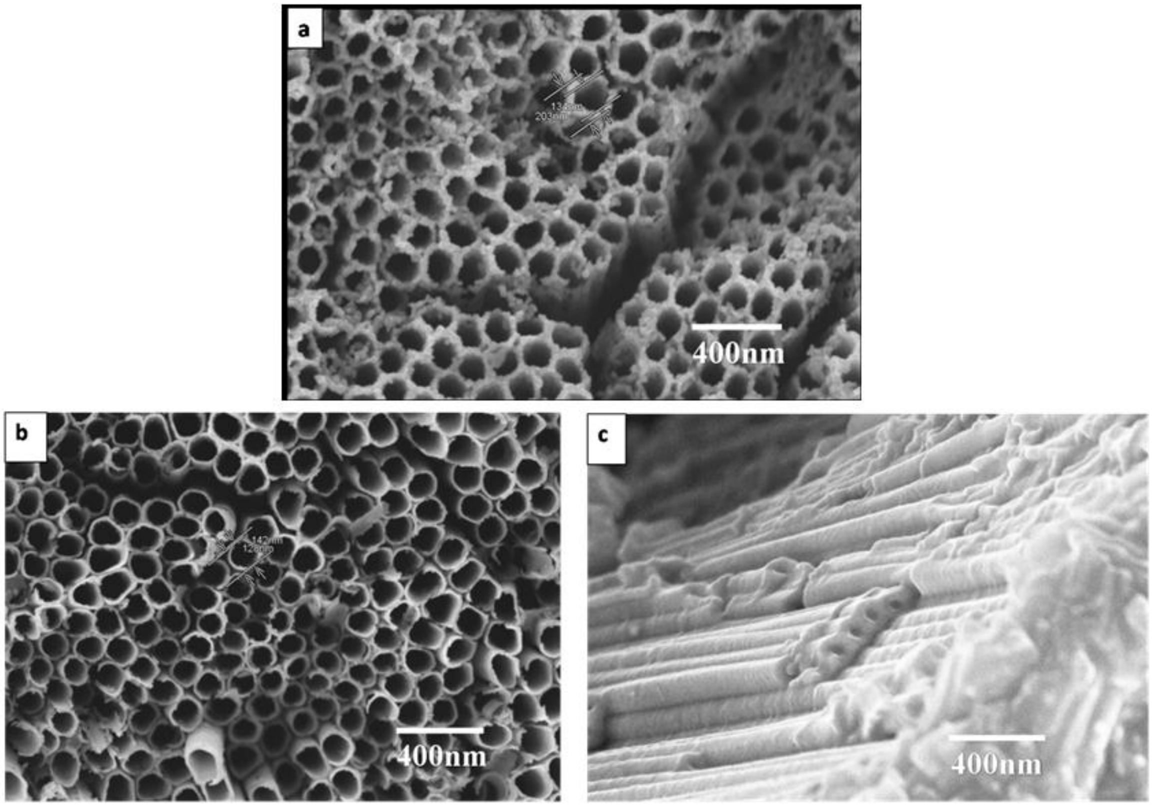

Figure 31 the SEM images of the titanium oxide nanotubes annealed under different treatment conditions. (a) 525^{o}C, atm., (b) 450^{o}C, atm. (c) 600^{o}C, 5×10^{-5}Torr

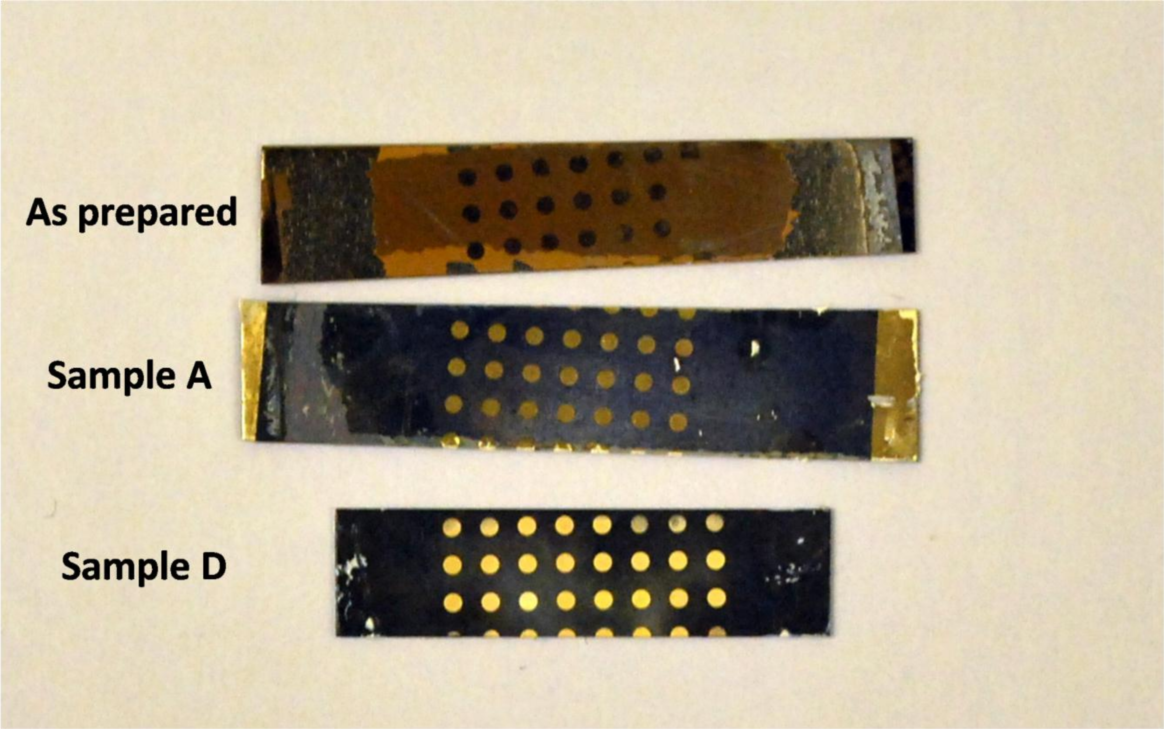

Figure 32 the photos of three samples with different colors. The upmost sample is "as-prepared"; the middle sample is Sample A; the undermost sample is Sample D.

The change of the charge carrier type of TiO2 nanotubes annealed under different atmosphere is possibly related to the crystal defect in it, which can be proven by the different color of samples. The stoichiometric TiO_2 is a yellow dielectric with low conductivity. However, TiO_2 can be easily reduced by forming oxygen vacancy after annealed under low oxygen partial pressure. The process can be described as the following reaction: [69]

$$2Ti_{Ti} + O_o \longrightarrow 2Ti_{Ti}' + V_o^{\bullet\bullet} + \frac{1}{2}O_2 \uparrow \tag*{11}$$

where Kroger's notations have been used.[70] Then it becomes an n-type semiconductor where the electron hopping between $^{\mathrm{Ti3+}}$ and Ti^{4+} contributes mainly to the total electric conductivity. Subsequently, $V_o^{\bullet\bullet}$ tends to capture electron to form color center, so that the color changes to black. The photos of three samples with different colors are shown in Figure 32. The as-prepared TiO_2 nanotube is yellowish, which implies the stoichiometry. After being annealed in air (Sample A), the samples turn gray and become an n-type semiconductor because the oxygen partial pressure is not sufficient and oxygen vacancies are formed. As the oxygen partial pressure is much lower in vacuum, the samples annealed in vacuum are even darker, which indicates the increase of the concentration of oxygen vacancies.

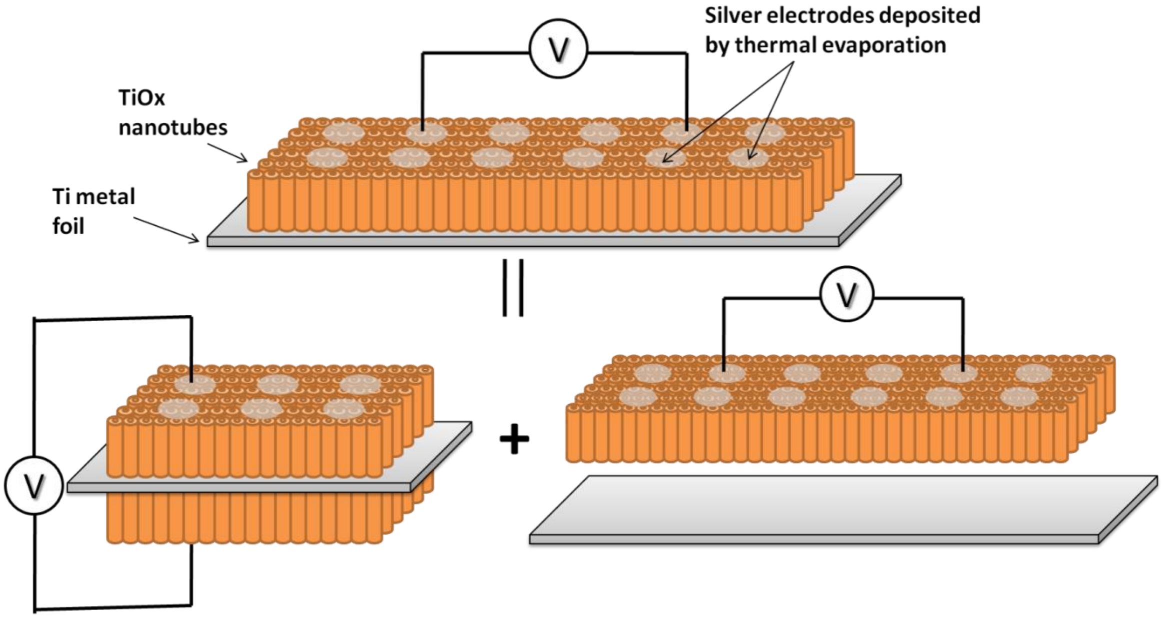

Figure 33 a schematic representation of the total thermopower contributions from both the nanotubes and the substrate.

In Figure 33, the thermopower contribution from the substrate is dissected. Without the lost of model validity, the thermoelectric voltage on the nanotubes-on-substrate sturcture can be treated as resulted from two contributions – one from the vertical direction, the other from the in-plane direction. The vertical direction contribution can be simplified to the structure on the bottom-left corner, which involves only temperature gradient in the vertical direction of the nanotubes; the in-plane direction contribution can be simplified to the structure on the bottom-right corner, which is seperated from the substrate and only involves cross-tube temprature gradient along the in-plane direction. The schematic break up of the orginal structure provides the fundation on which contribution from either of the directions can be determined qualitatively. If the barrier layer below the nanotubes has enough insulation, the thermoelectric voltage should follow a linear relationship with the temperature gradient in the planar direction. However, in the study, the thermoelectric voltage seems to be a combination of two, indicating that the substrate effect must be considered in the final discussion. Since Seebeck coefficient of the metal layer will be significantly smaller than that of the bulk, the sign of the Seebeck coefficient is solely determined by the bulk conduction properties.

Also worth noting is the fact that the Seebeck coefficient of the Ti substrate is measured to be positive, seemingly contrary to the conventional belief that it should be negative because the current is carried by electrons. The reason for Ti to have positive S is that, as the elctron-honon scattering rate increases more quickly with increasing temperature than does the mean velocity, the mean free path decreases. Therefore, the electrons migrate more easily from the cold side to the hot side, and bring about a positive value for Ti. The Seebeck coefficient is generally small on the Ti substrate compared with the nanotubes on top of it.

3.4 Investigation on the potential of organic semiconductor in thermoelectric applications

Light-emitting diodes (LED) has recently become one of the most promising commercially available display solutions in the world, with many advantages over their competitors that mostly use incandescent light sources. It is also widely used in many conventional applications such as automobile lighting, vessel lighting, aviation lighting, decorative lighting and traffic lighting, etc. They are very durable and reliable, highly energy efficient, and has faster switching rate. They can also be fabricated on flexible substrates, making it a promising candidate for the next generation flexible displays.[71] Above all, they are less expensive and have longer lifetime than most alternatives. However, one of the most prominent disadvantages of LED is the heating problem, resulting from the light emission process that involves an energy release process from the diode junction. This energy release will directly lead to two negative consequences. Firstly, during the operation of the LED, the accumulated energy induces a localized temperature rise on the LED itself, and this temperature increase will greatly reduce the power conversion efficiency, which is defined as the light output per unit power output (lm/W).[72] Secondly, the induced temperature increase will dramatically reduce the lifetime of the LED, making it less applicable to applications that require high reliability.[73] This heating problem had not been a prominent issue when LED was initially developed, but the ever increased requirement of making LEDs with higher luminous flux and brightness have driven the heat generation higher and higher. Therefore, many researchers have focused their efforts on the development of effective thermal management packages for the LEDs. Many of them used thermal packages based on the *Flip Chip* concept, which was widely used in the silicon based integrated circuits. In *Flip Chip* configuration, thermoelectric module can be used here to aid the dissipation of the heat generated by the junction and conducted by the heat spreader. Numerical simulation was used previously to validate the feasibility of employing thermoelectric cooler in place of the heat sink.[74] If effective thermoelectric cooling can be conducted, the LED array can be made even more compact, consuming even lower energy, and generating even higher brightness. Numerical study on the thermal management of LED packaging by using thermoelectric cooling have been investigated by Wang *et al.*[75] Their study, based on the finite element model of the LED packaging heat dissipation, demonstrated the effectiveness of the thermoelectric cooling module inside the package. They also found, via the simulation, optimal coefficient of performance (COP), heat resistance, and the dimensional parameters.

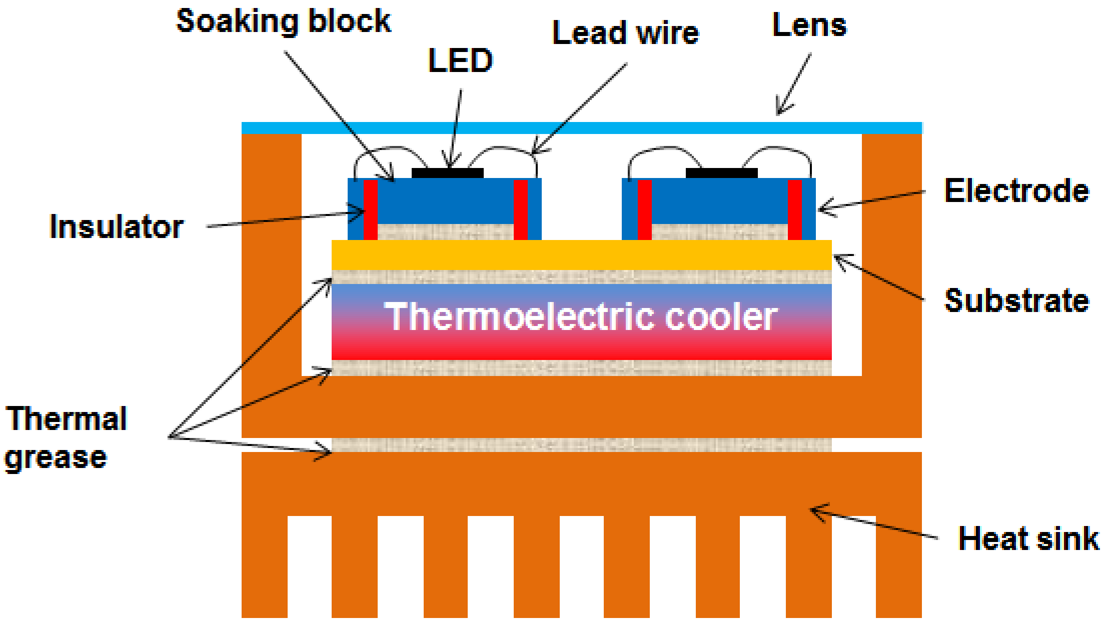

Figure 34 Schematic illustration of the LED packaging based on thermoelectric cooling system

However, finding a suitable thermoelectric material for dissipating the heat generated by LED is not a straightforward trial and error process. The selection of material is inevitably restricted by four factors. Firstly, specially designed heat dissipation channel is usually based on the heat conduction through the system board and the substrate, as in the popular *Flip Chip* configuration (Figure 35). Secondly, the thermoelectric would better be flexible, since one important direction for LED display evolution is the bendable display. Thirdly, the thermoelectric efficiency, evaluated by the thermoelectric figure-of-merit, $zT=S^2\sigma T/\kappa$, needs to be high enough to compete with other passive cooling alternatives. Lastly, the cost of the cooling module needs to be lower so that the overall manufacturing cost of the thermoelectric-module-cooled LED display does not exceed the current ones. In these regards, organic semiconductors, such as pentacene and rubrene, can be potentially good candidates. Recently, the Seebeck coefficient in thin films of pentacene and single crystals of rubrene has been successfully measured using field-effect devices at the temperature between 295 and 200K. The measured Seebeck coefficient falls into the range of 0.3 – 1 mV K^{-1}, and decreases logarithmically with increasing gate voltage. Earlier measurements on thermal transport properties in pentacene thin films and rubrene single crystals show room-temperature thermal conductivities of the order of 0.5 W m^{-1} K^{-1}. The relatively large Seebeck coefficient and low thermal conductivity indicate that these organic semiconductors can be potentially good thermoelectric materials. However, the difficulty in examining the potential of the organic semiconductor thermoelectric materials is that the electronic band structures of these materials are usually hard to be thoroughly understood, and so are their relationships with the Seebeck coefficient, the electrical conductivity and the thermal conductivity. Currently, organic thermoelectric materials have drawn little attention in thermoelectric property investigations.

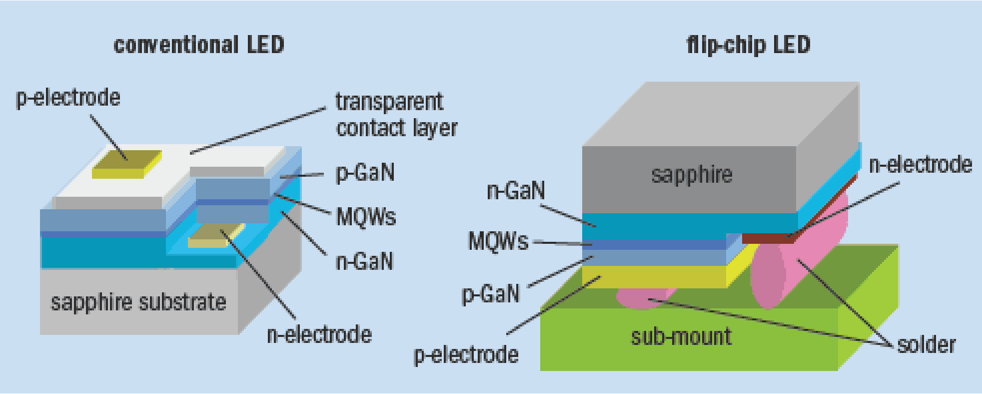

Figure 35 The flip-chip LED configuration as compared to the conventional structure for multiple quantum well (MQW) InGaN/GaN based light emitting diodes (LEDs).

(Source: T. Doan, *Compound Semiconductor*, 18 (2006))

In order to investigate the potential of the organic semiconductors as thermoelectric materials, D. Wang *et al* had done investigations on pentacene and rubrene, two widely used organic semiconductors by first-principles method,[76] which were also successfully used before by several researchers to discover potential materials that are suitable for thermoelectric applications.[77,78] The calculations of the electronic structure was coupled with the Boltzmann transport theory to study the thermoelectric properties of organic semiconductors, and the absolute values of the Seebeck coefficients were obtained. A peak zT value of 0.8-1.8 at 294K and 1.1-2.4 at 248K is calculated. For example, at 248 K, zT of pentacene exhibits a peak value of 1.1 and 2.4, evaluated, respectively, based on the room temperature mobility of 11.2 and 35 $cm^2\ V^{-1}\ s^{-1}$.

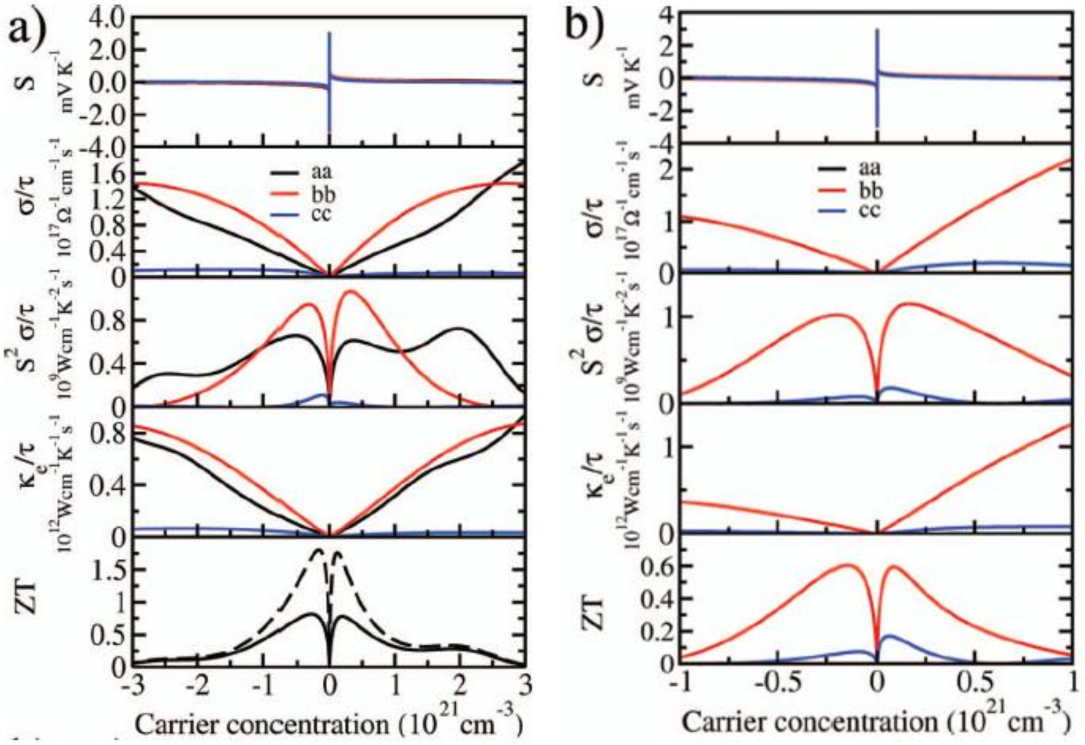

Figure 36 The thermoelectric properties of the organic semiconductors obtained by the first-principles calculations. (a) is pentacene and (b) is rubrene. From top to bottom are Seebeck coefficient, electrical conductivity, power factor, thermal conductivity and thermoelectric figure-of-merit.

(Source: D. Wang, L. Tang, M. Long and Z. Shuai, *J. Chem. Phys.*, 131, 224704, (2009))

These figures-of-merit, even at the lower limit, are close to those of the state-of-the-art thermoelectric materials. It indicates that organic materials can have great potentials as thermoelectric materials for near-room-temperature applications such as environment-friendly refrigeration. Analysis of the band structures in pentacene and rubrene shows that the good thermoelectric properties rely on the simultaneous presence of both flat and dispersed bands around the Fermi level.

Although the first-principles investigations, coupled with Boltzmann transport equations, had envisioned the possibility of practical applications of organic semiconductors in thermoelectric cooling devices on LEDs, the major difficulty remains in the fabrication of such organic materials to reach the theoretical prediction. Currently, the best materials available are the alloys of bismuth tellurides with certain levels of doping by other elements, but the highest zT is only ~1.2 at room temperature, as is experimentally produced and verified by Beyer *et al* in their studies on PbTe and Bi_2Te_3-based superlattices.[79] In terms of Carnot efficiency, a zT of 1 only accounts for 10% of total energy conversion efficiency. In order to reach a Carnot efficiency of 30%, similar to that of a commercialized refrigerator, a device needs to have a thermoelectric zT of 4.[80] Despite of the recent advances, the great gap in efficiency between the conventional thermoelectric materials and the vapor-compression refrigeration systems remained a great challenge for the extensive commercialization of the thermoelectric devices. For organic semiconductors however, since the fabrication cost is significantly lower than their inorganic counterparts, their disadvantages in the figure-of-merit can be considerably offset by their advantages in cost, flexibility, large area fabrication ability, transparency, etc. If the organic semiconductors can be fabricated and doped to have comparable zT to their inorganic counterparts, the potential would be very attractive.

3.5 Oxygen Doping to Enhance the Thermoelectric Power Factor and Electrical Conductivity of Organic Semiconductors

For inorganic semiconductors high thermoelectric performance was obtained by fine-tuning the doping level of the compounding materials,[79] but for the organic semiconductors, the details of the doping mechanism of oxygen to p-type organic semiconductors are not yet well understood. For example, when we consider the energy diagram of an organic semiconductor and an oxygen molecule system, the energy separation between the highest occupied molecular orbital of the organic semiconductor and the lowest unoccupied molecular orbital of an oxygen molecule is much larger than the thermal energy at room temperature; Lu *et al* have shown that the electron affinity of an oxygen molecule is 0.45 eV in the gas phase, and the typical ionization potential of p-type organic semiconductor s is in the range from 5 to 6 eV.[81] Even if the energy difference in O_2 between in gas phase and in organic semiconductor solids is taken into account, the energy required for the electron transfer from the organic semiconductor to oxygen is still much larger than kT. When the oxygen anion and the cation of the organic semiconductor can be bound to gain an attractive Coulomb potential, the energy barrier for electron transfer can become smaller, making electron transfer possible. However, the formed cation is strongly bound by the oxygen anion due to the large Coulomb potential, resulting in no effective generation of mobile holes. This point suggests that excess energy is necessary for effectively creating mobile carriers. Ogawa *et al* found that the charge transfer between pentacene and oxygen molecules is significantly enhanced by exposure to both oxygen gas and light.[82] This photo-induced doping effect induces a drastic shift in the threshold gate voltage for hole accumulation at the channel along with a distinct change in the FET properties, suggesting that the electron transfer from a pentacene molecule to an oxygen molecule effectively occurs through the excitation of the pentacene molecule by light absorption. Figure 37 shows the transfer characteristics of the device exposed to illumination, with and without oxygen’s existence. The device showed a dramatic shift of the transfer curve to the upper right direction when it was exposed to both the illumination and the oxygen. On the contrary, without oxygen's presence, the illumination itself had little effect in changing the organic thin film transistor's electrical properties. This result is an important indication towards the effectiveness of organic semiconductor modification. Specifically, with the combining effect of the illumination and oxygen, and thus the photo-oxidation, the electrical conductivity of the film at zero gate bias can be greatly improved.

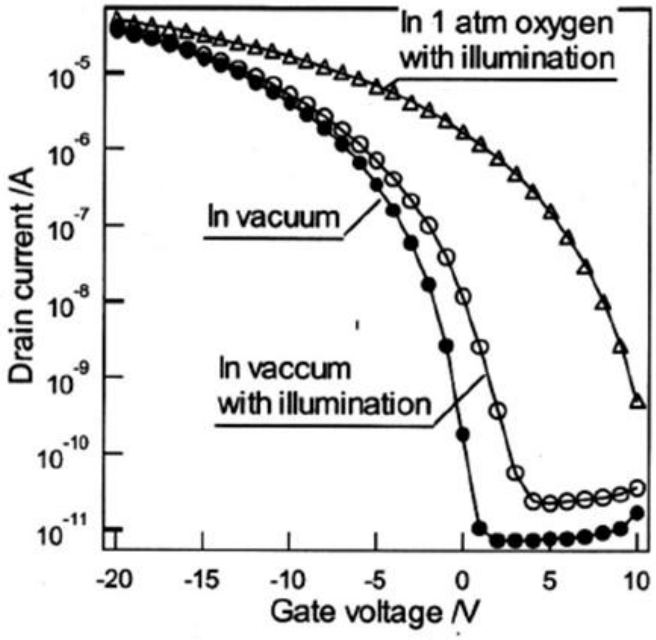

Figure 37 A comparison of the transfer characteristics of the same pentacene OTFT under different conditions: in vacuum without illumination; in vacuum with alumination; and in atmosphere with illumination.

(S. Ogawa, T. Naijo, Y. Kimura, H. Ishii and M. Niwano, *Appl. Phys. Lett.*, **86**, 202104 (2005))

The above indication is essentially important to the idea of thermoelectric property modifications. In typical organic semiconductors such as pentacene and rubrene, the Seebeck coefficient is related to the electrical conductivity in a complicated way which involves the change of Fermi energy level and the introduction of excess hole traps. The general pattern, however, is known as a reverse relationship. With the increase of the Seebeck coefficient, the electrical conductivity is sacrificed. This is why the researchers have made numerous efforts in enhancing the power factor $S^2\sigma$. For thermoelectric applications like LED cooling as mentioned above, a promising method is to increase the electrical conductivity of the film without much sacrifice from the Seebeck coefficient. Therefore, doping the thin film to make it more conductive at zero bias by photo-oxidation had caught the interest of some researchers. Among them, Chabinyc *et al* have tested the effect of ozone on polythiophene-based thin-film transistors and found surprising results.[83] The effects of the exposure of the thiophene-based thin-film transistors TFTs to the ambient atmosphere, oxygen, and ozone were investigated. The off-state current increased and the threshold voltage became more positive when the TFTs were exposed to the ambient. Exposure to purified air along, however, did not change the characteristics of TFTs. The results shown in Figure 38 suggested that the ozone could actually be the source that caused the abovementioned off-state current increase and threshold voltage shift, because the ozone treated sample (represented by gray line) deviates dramatically from the fresh sample (represented by black line), as well as the annealed sample (in nitrogen, represented in black dots). Density functional calculations showed that ozone forms a complex with polythiophene, that is, a shallow acceptor.[83] These results indicate that ozone in the ambient is the cause for the changes in electrical characteristics of polythiophene-based TFTs rather than oxygen. Although this set of experiments did not cover other organic semiconductors such as pentacene and rubrene, it opens the possibility that similar enhancement can be found upon those materials by ozone treatment.

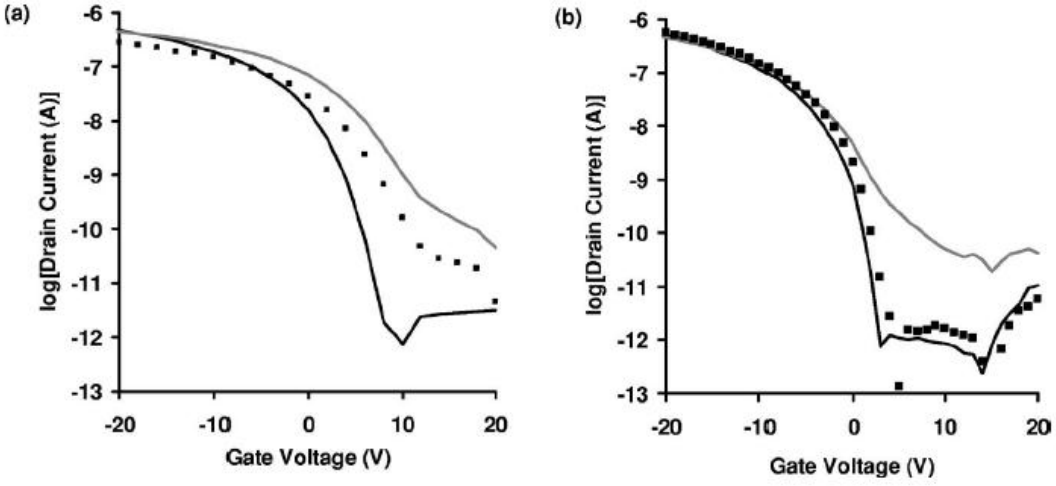

Figure 38 Current-voltage characteristics measured in the linear regime. The devices (a) PQT-12 and (b) PBTTT-C14 were measured after fabrication (black line), after brief exposure to 1–10 ppm ozone in dry air (gray line), and after annealing at 100 °C in nitrogen (black squares).

(Source: M. L. Chabinyc, R. A. Street and J. E. Northrup, *Appl. Phys, lett.*, **90,** 123508 (2007))

3.6 Charge Injection and Transport in Organic Semiconductors

The above indication of potential enhancement of electrical conductivity of organic thin film is prospective, but the actual carrier transport within the metal-organic-metal type of devices also depends heavily on the bulk properties and the interface properties. Enhancing the electrical conductivity of organic thin films does not simply conform to the SCL injection scenario. One objective of this chapter is to investigate the interface factors and provide theoretical predication on the enhancement of the electrical conductivity and thermoelectric power factors of the organic semiconductors. In addressing the carrier injection complication that involves hole injection from metal to a hopping system like pentacene, a model developed by Arkhipov *et al* is used as a reference based on which our model is built.[84] In their work they presented an analytical approach to the abovementioned problem in conjunction with experimental data. The basic conclusion was that dark injection can be understood in terms of field effect and the temperature gradient that drives the charge to move between the metal-dielectric interfaces. At an arbitrary distance x away from the metal-polymer interface, located at x=0, the electrostatic potential of a carrier relative to the Fermi level of the electrode is given by the superposition of the image potential, the external potential and the site energy E,[84]

$$U(x,E)=\Delta-\left(\frac{e^2}{16\pi\epsilon_0\epsilon_x}\right)-eF_{ox}+E \tag{12}$$

where F_0 is the external field strength, e the elementary charge, ϵ the electric constant, and ϵ_0 the dielectric permittivity. The injection current density, j(t), can be written as[84]

$$j_{inj}=ev_0\int_a^\infty dx_0\exp(-2\gamma x_0)w_{esc}(x_0)\times\int_{-\infty}^{\infty}dE'Bol(E')g[U_0(x_0)-E'] \tag{13}$$

where w_{esc} is the probability for a carrier to be deprived of recombination, v_0 is the attempt-to-jump frequency, γ the inverse localization radius, and the function $Bol(E)$ is defined as,[84]

$$\begin{aligned}&Bol(E)=\exp\left(-\frac{E}{kT}\right),E>0\\&Bol(E)=1,E<0\end{aligned} \tag{14}$$

The carrier escape probability w_{esc} can be solved by[84]

$$w_{esc} = \frac{\int_{a}^{x_0} dx \exp\left(-\frac{e}{kT}\left(F_0 x + \frac{e}{16\pi\varepsilon_0\varepsilon}\frac{1}{x} \right) \right)}{\int_{a}^{\infty} dx \exp\left(-\frac{e}{kT}\left(F_0 x + \frac{e}{16\pi\varepsilon_0\varepsilon}\frac{1}{x} \right) \right)} \qquad \mathbf{15}$$

This value, as can be seen from the difference between the numerator and denominator, strongly depends on the distance x_0, the minimum value being the intersite distance a, which is typically 0.6nm for pentacene. Figure 39 shows a series of current-field characteristics for pentacene thin films in the normal operation ranges for an in-plane thermoelectric device. The injection current increases intuitively with decreasing Δ and with electric field. As the energy barrier increases linearly from 0.2eV to 0.6eV, the injection current decrease in an accelerated rate. For DOS variance at 0.08eV, the barrier height has the most significant impact on the injection current, with Δ>0.6eV yields injection current lower than 1×10^{31}A current at the field of 1×10^{5} V/m. The DOS variance means the energetic distribution of the holes within the pentacene, so with a wider distribution, a larger σ, the injection current is generally larger, and relatively unaffected by the barrier height. This is also intuitive as the wider distribution of energy brings more carriers over the barrier height. From (a) to (c), as the energy variance increases, the injection current shows a convergence to a high injection current point, indicate by its logarithmic scale.

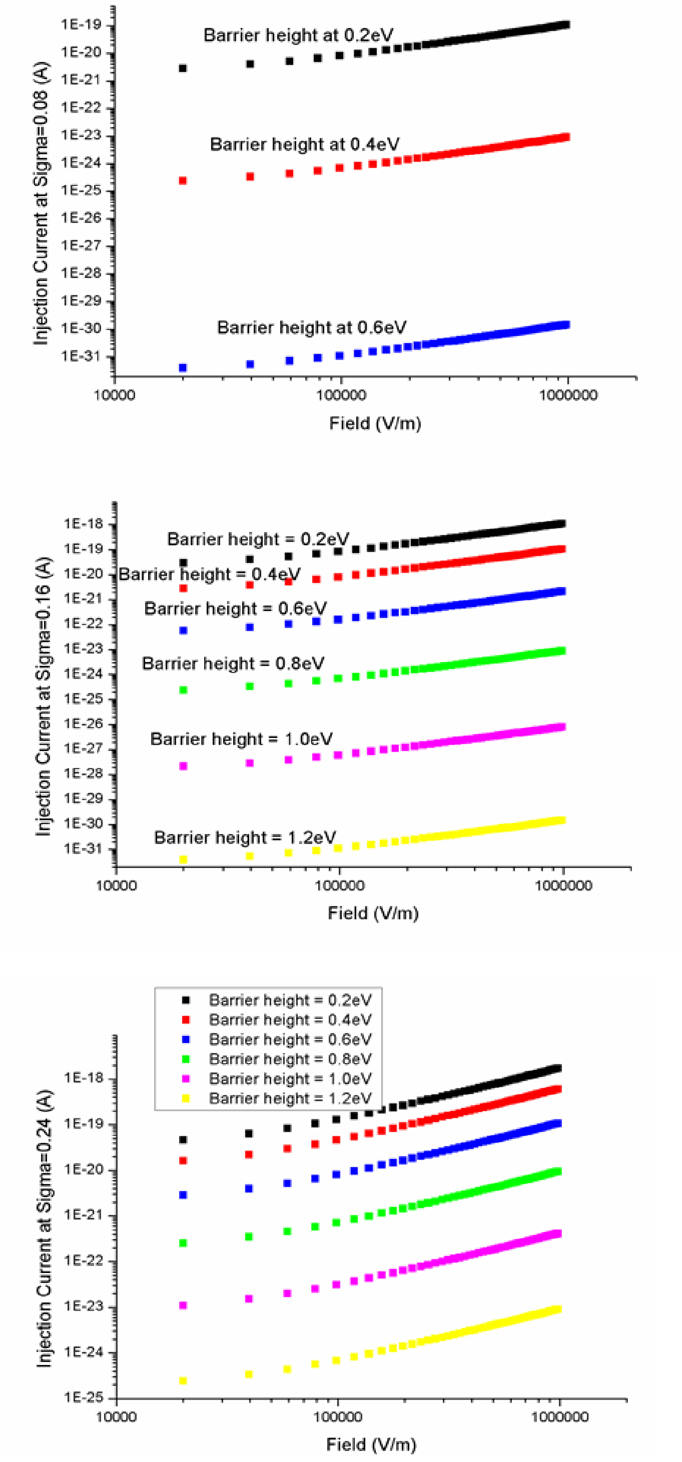

Figure 39 Injection current as a function of field. This is illustrative of the charge carrier injection across a barrier of height Δ into an energetically and positionally disordered hopping system characterized by energetic variance (a) σ=0.08eV, (b) σ=0.16eV, (c) σ=0.24eV and a minimum intersite distance a=0.6nm for pentacene at 300K

The temperature dependence is shown in Figure 40. The injection current into pentacene is temperature dependent, with the temperature dependence decreasing strongly with increasing electric field. However, the temperature dependence is not considered strong at Δ=0.4eV and variance σ=0.08eV. For the field-current relationship, as the field increases, the temperature dependence drops significantly. This indicates that at the normal operating range of an LED cooler (300K-400K), the injection current will mostly affected by the field rather than the temperature. In addition, since the lg.field-lg.current curves shows a concave shape, the field increase will positive affect the charge carrier injection, and thus the electrical conductivity of the film. The reason is that, the smaller device can have larger field and since their conductivity is injection limited, it positive responds to the field.

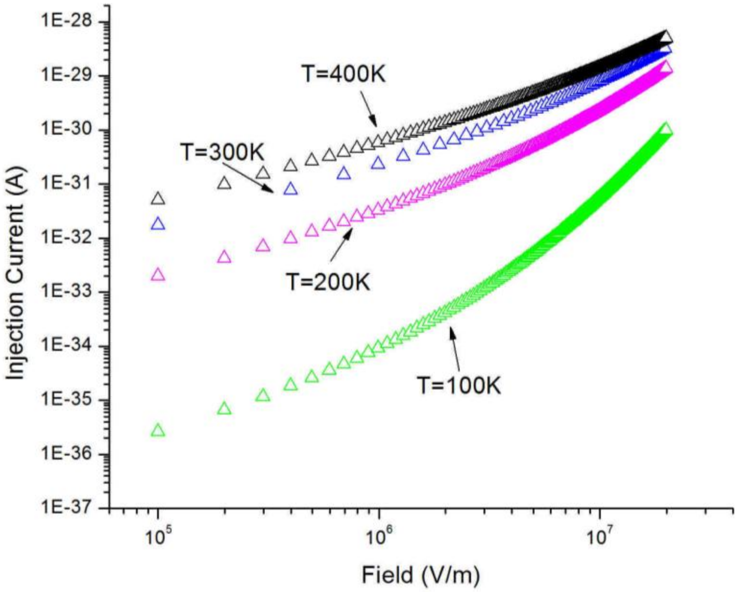

Figure 40 Temperature dependence of current vs field characteristics for carrier injection across a barrier of Δ=0.4eV into a disordered hopping system (pentacene) characterized by the energy variance σ=0.08eV

Disorder has a prominent effect on the injection efficiency as borne out by Figure 41. As can be seen, the current increases significantly as the width of the distribution increase, the more so when the larger the injection barrier is. This means that the injection of charge carriers into an organic hopping system is a combined process. In a pentacene thin film with metal electrodes, the larger the spread of the site energies, the more likely it becomes for a carrier to find an acceptor site at an energy less that the barrier height. This provides us with a framework to design the device. The general tendency to increase the pentacene carrier injection and transport is to avoid traps that increases that energy difference. This will also be reflected on the transfer characteristics as the traps of pentacene tend to move the threshold voltage to the negative direction, making zero-bias current smaller.

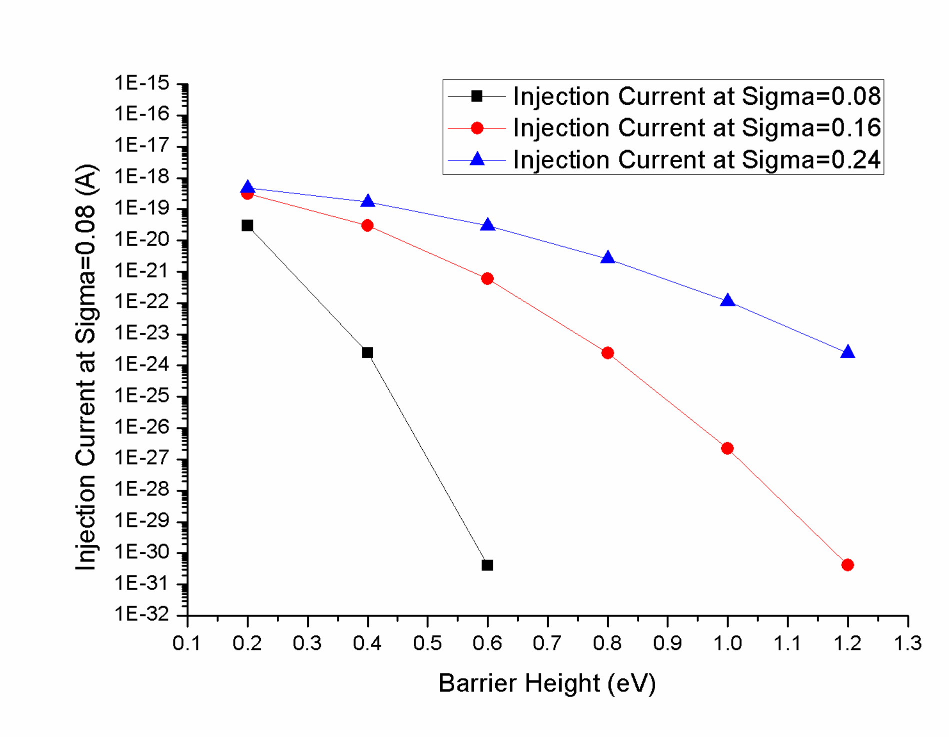

Figure 41 Dependence of injection current on barrier height Δ for variable widths of the distribution of the density of hopping sites

3.7 Conclusion

This chapter discusses the enhancement of Seebeck coefficient in two different materials with different methodology.

In titanium oxide, aside from the Seebeck coefficient's enhancement by the nanotube structure and its dependence on the treatment conditions and the measurement temperatures, more interesting findings were found along the investigation. The first is the change of charge carrier type from conventional n-type to unconventional p-type. The change of sign indicates the effect of vacuum annealing on the oxygen vacancies in the titanium oxide nanotubes. The mechanism for this change was discussed along with the effect of the Ti metal substrate, which is hard to be seperated with the nanotube structure. The second finding is the morphology change following a pattern that wallthickness increases with the increase of annealing temperature and the increase of vacuum level. Total nanotube melting was observed for elevated annealing temperature in the vacuum condition. The third is the pattern of change of Seebeck coefficients against the measurement tempeatures. With the increasing measurement temperature, the magnitude of S genreally increases for atmospheric annealing but decreases for vacuum annealing. An optimal S is also found in the 525C atmospheric annealing condition. Future work could be carried out upon finding the transition temperature by varying the annealing conditions. There should be an intermediate annealing condition which gives that temperature, with which the tranport properties including carrier concentration and density of states can be further investigated. Last but not the least, patterning and transferring techniques can be utilized in order to transfer the nanotube arrays onto an insulating substrate. This will further eliminate the extrinsic influence from the metal substrate.

For organic thin film, however, the scenario is a bit different, because although indication of potential enhancement of electrical conductivity of organic thin film is prospective, the actual carrier transport within the metal-organic-metal type of devices also depends heavily on the bulk properties and the interface properties. The model used in this chapter focuses on the interfacial effect of the organic thin film, which is injection-based. As the energy barrier increases linearly, the injection current decrease in an accelerated rate. The DOS variance means the energetic distribution of the holes within the pentacene, so with a wider distribution, a larger σ, the injection current is generally larger, and relatively unaffected by the barrier height. More than that, the current increases significantly as the width of the distribution increase, reflecting that the injection of charge carriers into an organic hopping system is a combined process. In a pentacene thin film with metal electrodes, the larger the spread of the site energies, the more likely it becomes for a carrier to find an acceptor site at an energy less that the barrier height. This provides us with a framework to design the device. The general tendency to increase the pentacene carrier injection and transport is to avoid traps that increase that energy difference. This will be highly useful when effort is made upon the fine-tuning of the threshold voltage by trap control.

4. Conclusions, Challenges and Future Directions

4.1 Conclusion

In this thesis, the thermoelectricity of the small-molecular-weight organic semiconductors has been investigated, along with that of the nanostructure in the form of titanium oxide nanotube array. The studies have been unfolded in two primary directions.

The first direction is using the thermoelectric effect to non-destructively characterize the effective channel thickness of the organic thin film transistors. This study is based on the Boltzmann Transport Theory, using the correlation of the Seebeck coefficient with the charge carrier transport properties, including the areal and volumetric carrier density, the effective density of states, the threshold voltage, and the gate voltage. The data have shown that the charge carrier density can be effectively modulated by external fields created by the imposed biases on the gate of the OTFTs, and the carriers tend to concentrate close to the dielectric interface when the field effect is enhanced. The concentration profile deviates from the Debye length prediction because of the layer-by-layer deposition nature of the organic semiconductor molecules. These results are used in evaluating the effective channel thickness of the OTFTs under different operating bias, which can be very useful in production-related applications. In such applications, the film thickness of the channel can be precisely controlled by the effective channel thickness predicted by this method.

The second direction is the enhancement of the thermoelectricity of pentacene and titanium oxide. Because of the dramatically different nature of the organic pentacene and the inorganic titanium oxide, different enhancement methods have been applied. For pentacene, ozone treatment was studied and generated inconclusive fluctuating results, albeit observable enhancement in the short treatment time regime. In order to seek a theoretical explanation to the enhancement, a metal-organic charge carrier injection model is used, based on which a series of parameters are modified. The results have shown that the excessive ozone treatment may have created too many deep traps that impede the improvement on the electrical conductivity, and thus the thermoelectric power factor for the organic semiconductor thermoelectric device. For the titanium oxide, nanotube structure is used as a way to enhance the thermoelectric property. The Seebeck coefficient of the nanotubes with different annealing conditions are measured and compared. Besides the general trend of the enhancement of Seebeck coefficient by annealing temperature, an interesting change of sign in the Seebeck coefficient is found in the samples annealed in vacuum.

Overall, the primary goal of this thesis, that is, the investigations of thermoelectric properties on the semiconductors have been realized, and a handful of applications have been discussed. The results of this thesis can serve as a foundation based on which further improvements on the thermoelectric measurement, enhancements and effective-channel-thickness related applications.

4.2 Unaddressed issues and future directions

Despite the revelation of the carrier transport and thermoelectric properties, there are still a few unaddressed issues or challenges in the studies as described above.

The first issue is in the thermoelectric enhancement of titanium oxides by nanotube structure. While the enhancement in Seebeck coefficient is observed compared to thin film results previously obtained by other researchers, the enhancement of the thermoelectric power factor and the thermoelectric figure of merit are not investigated. It would be possible for the other two parameters to vary in their relationships to the nanotube structure and different treatment condition. Also, the results are under-representative if substrate effect is involved. Although in our discussion, the substrate effect has been proven to have negligible effect for Seebeck coefficient evaluation, it would have great effect for electrical and thermal conductivity measurements. Therefore, it presents much difficulty in the assessment of the nanostructure's effect on the thermoelectric effect enhancement. One of the potential modifications can be on the substrate itself. As can be seen in Figure 42, the nanotube array's cracks are unlikely to be formed by the thermal treatment after the fabrication, but likely by the anodization process. During the anodization process, the cracks are already formed so that the solution can penetrate down to the substrate and leave some discontinuous oxide patterns on the substrate, distinct from the nanotubes' leftover. A possible explanation is that, since the anodization is not performed at a uniform rate on the surface of the Ti metal – caused by the tiny fluctuation of the voltage and the movement of liquid in the beaker – some part of the substrate is anodized at a faster rate than the others and causes internal stress in the sample, inducing tiny cracks and preventing the nanotubes from growing in a highly ordered manner.

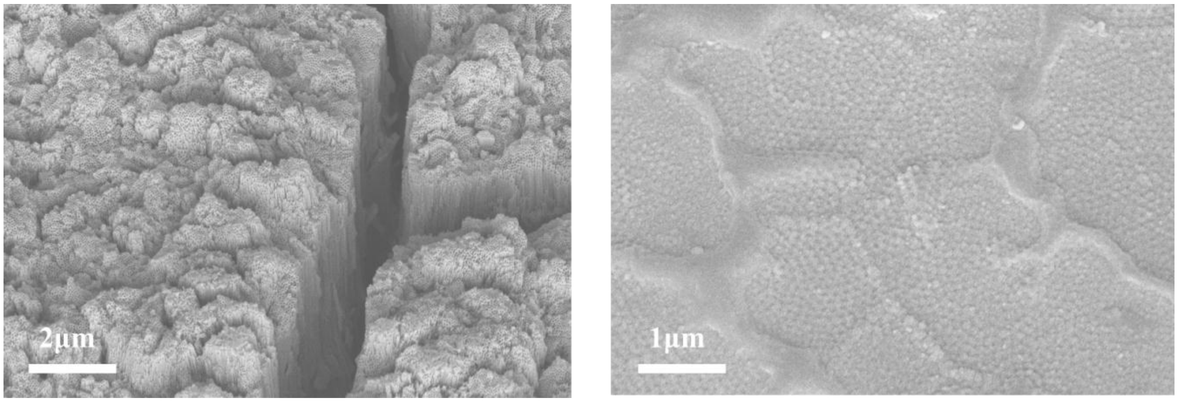

Figure 42 The SEM images of the pervasive tiny tracks on the nanotube arrays (left) presents difficulties for accurate thermoelectric properties evaluation. But this is unlikely a problem caused by the thermal treatment steps as the cracks have induced discontinuous oxide formation on the substrate itself (right), which can only happen during the anodization process.

The solution of this problem can be using a silicon-wafer-based substrate instead of the Ti metal. The silicon-wafer-based substrate needs to be pre-processed by depositing a uniform and dense Ti metal layer on top of it, and the anodization can be performed on this substrate to avoid any stress-induced cracks. This process is illustrated in Figure 43. In this three step fabrication process, a silicon dioxide film is firstly grown on the silicon substrate, the surface of which is flat enough for titanium to be deposited on it. Secondly, a titanium metal film is deposited by thermal evaporation or pulse laser deposition. The thickness of the film should be controlled to be around 50μm, which is the length for the titanium oxide nanotubes to be uniformed arranged, such as those fabricated in Chapter 3. Thirdly, potentiostatic anodization is conducted on the sample based on the same procedures as described in Chapter 3. The duration of the anodization is supposed to be critical to the quality of the nanotube array because of the thickness of the metal film, because excessive anodization might damage the nanotube structure of the titanium oxide.

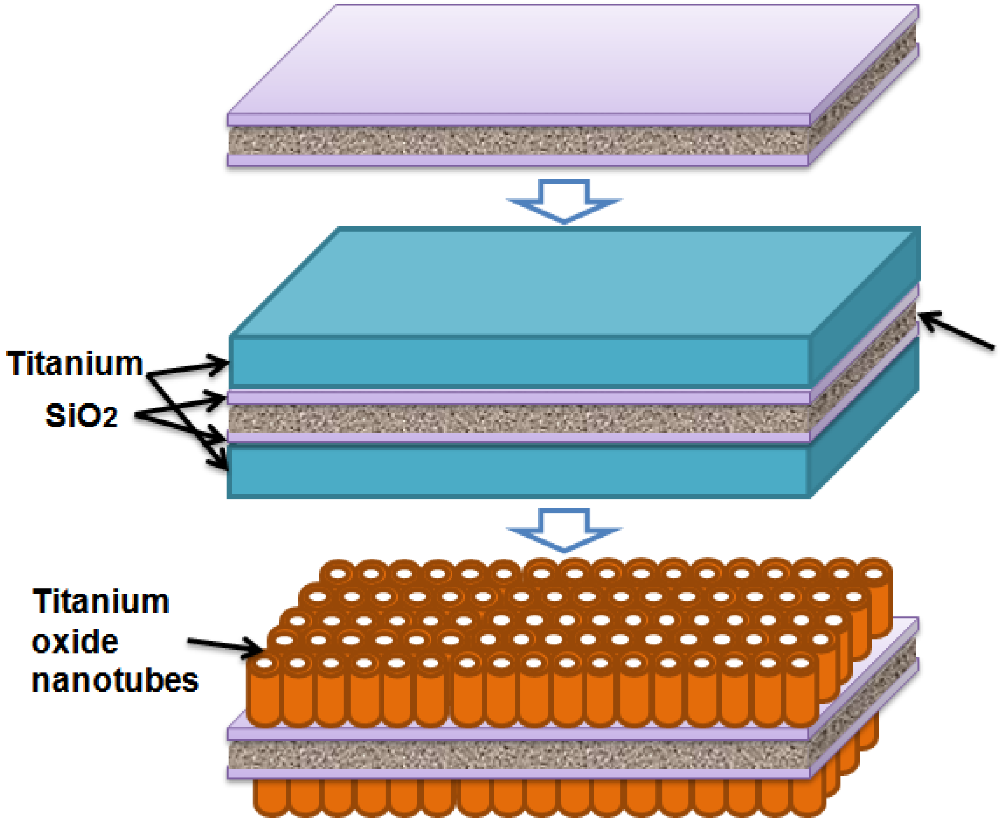

Figure 43 Illustration of the process of titanium oxide nanotube fabrication on silicon wafers to prevent cracks.

The nanotube array fabricated using this method would ensure that the substrate remains flat during the fabrication process. Therefore, the internal stress of the nanotube array would be dramatically reduced, and so is the number of cracks. The consequential carrier transport would be relatively defect-free and the measured Seebeck coefficient would more accurately reflect the actual Seebeck coefficient of the titanium oxide nanotubes.

The second unaddressed issue is that, for the effective channel thickness measurement, the charge traps created during the experimental process induces some uncertainties on the results. Since the traps are strongly related to the threshold voltage, which is in turn associated with the carrier density calculation, the accuracy of the effective channel thickness evaluation was affected. This could be solved by using HDMS-based or other types of dielectric treatment techniques that shift the threshold voltage in the positive direction. Figure 44 shows the impact of different dielectric surface treatment methods on the threshold voltage of pentacene OTFTs.[85] It can be observed that for C, E and F, there exist an apparent increase of off-state current for the OTFT, indicating an enhancement of mobile charge carrier concentration at zero bias. Future experiments can be conducted in this regard as to use the changed mobile charges to subdue the trap states that cause the threshold voltage's shift in the negative direction.

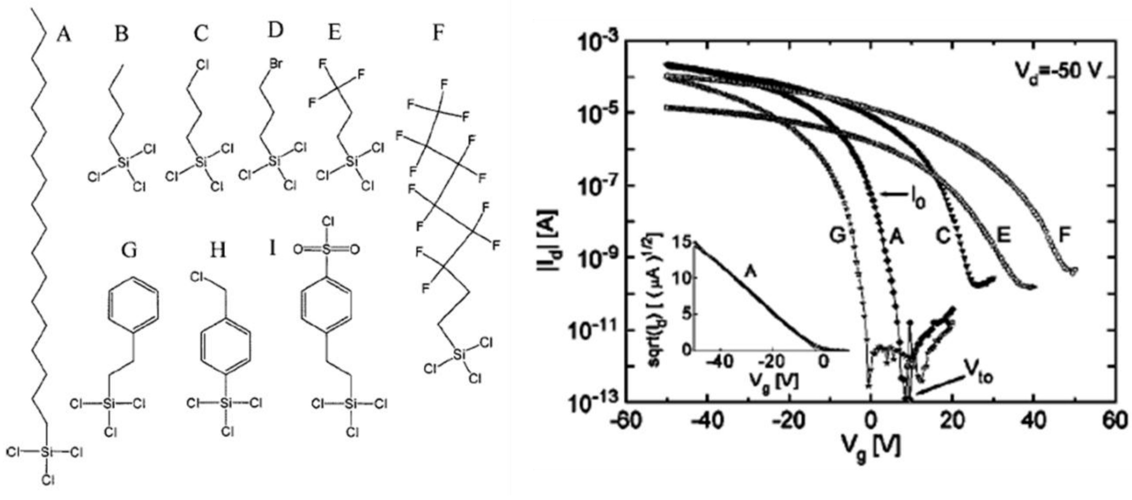

Figure 44 Surface treatment using different organic solutions have great impact on the threshold voltage of the pentacene OTFT, with their molecular structures shown on the left, and their respective effect on the threshold voltage shift shown on the right. The increase of the off-state current indicates the presence of mobile charges at zero gate bias.

(Source: K. P. Pernstich, S. Haas, D. Oberhoff, C. Goldmann, D. J. Gundlach, B. Batlogg, A. N. Rashid and G. Schitter, *J. Appl. Phys.*, **96,** 11 (2004))

Thirdly, for the enhancement of Seebeck coefficient in the organic thin films, the model has some uncertainties in predicting the electrical conductivities. In the experiments, the electrical conductivities are over one order greater than the predicted conductivities under the same electric field. There are two reasons that can cause the problem. The first is that the metal to hopping system injection model used in this thesis is not able to address large scale devices because it was customized for small-distance-large-field scenarios. The second is that the hole traps created during the fabrication procedure warped the experimental results, making electronic conductivity in unbiased environment larger than it was intrinsically. To address this issue, organic single crystal should replace the thin film, of which the intrinsic contribution from the electronic conductivity is unavoidably introduced. However, as our experiences with the organic single-crystal-based field effect transistors have shown, the most challenging part is to make good contact between the organic – in our case, rubrene – single crystal and the silicon substrate. This is because the rubrene single crystals are fabricated in a uncontrolled environment (in terms of shape and position of the crystals), so it's a-b surface was not flat enough (>100nm) for the field effect to take effect inside the single crystal. Therefore, *in-situ* growth of single crystal, as illustrated in Figure 43 is a potential solution to the above unaddressed issue. In this proposed scheme, organic single crystals are grown on the prefabricated metal electrodes *in-situ*, conducted in an enclosed quartz tube filled with moving nitrogen laminar flow. The temperature gradient is supplied by the three-zone furnace, and ensured that the purified organic semiconductor power were heated to the temperature a little higher than the sublimation temperature, and that the single crystals are formed on the substrate placed inside the tube in advance. Organic single crystals are not necessarily formed directly across the channels but there is a probability for some of them to be right across them. Subsequent clearing steps can be applied to remove the unnecessary crystals and ensure that one channel only corresponds to one single crystal.

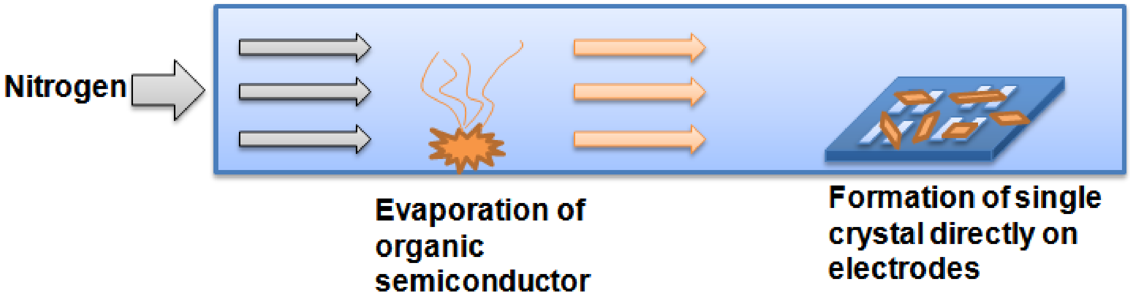

Figure 45 Schematic illustration of proposed direct growth of organic single crystal on prefabricated metal electrodes.

By applying in-situ growth of the organic single crystals, the contact between the metal electrode and single crystals are ensured in the bottom contact organic single crystal field effect transistors. The interface-borne carrier traps would be removed as compared to the conventionally fabricated transistors. Also, compared with the thin film transistors, the intrinsic carrier transport properties are no longer hindered by the numerous grain boundaries, and the measured Seebeck coefficient would be much more accurate in reflecting the intrinsic values of the corresponding organic semiconductors.

References

---

[1] K. P. Pipe, *Bipolar Thermoelectric Devices*, pp.22 MIT, (2004)

[2] R. Smith, *Semiconductors*, (Cambridge University Press, London, (1980)

[3] Pope, C. E. Swenberg, *Electronic Processes in Organic Crystals and Polymers*, 2nd ed., Oxford University Press, Oxford, 337 (1999)

[4] S. W. Tang, H. Fu, R. Wang, J. Lu, K. Yu and Y. Tao, *Appl. Phys. Lett*., **95**, 183505, (2009)

[5] N. Li and S. Forrest, *Appl. Phys. Lett*., **95**, 123309, (2009)

[6] I. W. Wu, Y. H. Chen, P. S. Wang, C. S. Wang, C. G. Wang, S. H. Hsu and C. I. Wu, *Appl. Phys. Lett*., **96**, 013301, (2010)

[7] R. R. Lunt, B. E. Lassiter, J. B. Benziger, and S. R. Forrest, *Appl. Phys. Lett.*, **95**, 233305, (2009)

[8] S. H Li, Z. Xu, G. Yang, L. Ma and Y. Yang, *Appl. Phys. Lett.*, **93**, 213301, (2008).

[9] T. Kawanishi, T. Fujiwara, M. Kasaya, A. Saito, M. Aono, J. Takeya and Y. Kuwahara, *Appl. Phys. Lett.*, **93**, 023303, (2008).

---

[10] T. Sekitani, T. Yokota, U. Zschieschang, H. Klauk, S. Bauer, K Takeuchi, M. Takamiya, T. Sakurai and T. Someya, *Science*, **236**, 1516, (2009).

[11] C. W. Tang, S. A. Van Slyke, *Appl. Phys. Lett.*, **51**, 913, (1987).

[12] J. H. Burroughes, D. D. Bradley, A. R. Brown, R. N. Marks, K. Mackay, R. H. Friend, P. L. Burn, A. B. Holmes, *Nature*, **347**, 539, (1990).

[13] D. M. Burland, U. Konzelmann, *J. Chem. Phys.*, **67**, 319, (1977)

[14] K. Kudo, M. Yamashina, T. Moriizumi, *Jpn. J. Appl. Phys.*, **23**, 130, (1984).

[15] A. Tsumura, H. Koezuka, T. Ando, *Appl. Phys. Lett.*, **49**, 1210, (1986).

[16] F. Ebisawa, T. Kurokawa, S. Nara, *J. Appl. Phys.*, **54**, 3255, (1983).

[17] R. H. Friend, J. Burroughes, T. Shimoda, *Phys. World*, **12**, 35, (1999).

[18] M. Shtein, J. Mapel, J. B. Benziger and S. R. Forrest, *Appl. Phys. Lett.*, **81**, 268, (2002).

---

[19] Y. D. Park, D. H. Kim, Y. Jang, M. Hwang, J. A. Lim and K. Cho, *Appl. Phys. Lett.*, **87**, 243509, (2005).

[20] E. Menard, V. Podzorov, S.-H. Hur, A. Gaur, M.E. Gershenson and J.A. Rogers, *Adv. Mater.*, **16**, 2097, (2004).

[21] I. Yagi, K. Tsukagoshi, and Y. Aoyagi, *Appl. Phys. Lett.* **84**, 813, (2004).

[22] K. P. Pernstich, B. Rossner, and B. Batlogg, *Nature Mater*. **7**, 321, (2008)

[23] D. Wang, L. Tang, M. Long, Z. Shuai, *J. Chem. Phys.* **131**, 224704 (2009)

[24] Y. Okada, M. Uno, and J. Takeya, *Mater. Res. Soc. Symp. Proc.* **B10**, 1154, (2009)

[25] N. Carl, *Synthetic Metals* **133**, 649–657, (2003)

26 A. Dodabalapur, L. Torsi, H. E. Katz, *Science* **268**, 270 (1995).

[27] S. M. Sze, *Physics of Semiconductor Devices*, Wiley, (1981).

[28] M. Mottaghi and G. Horowitz, *Org. Elec.*, **7**, 528, (2006).

---

[29] N. Yoneya, M. Noda, N. Hirai, K. Nomoto, M. Wada and J. Kasahara, *Appl. Phys. Lett.*, **85**, 20, (2004).

[30] L. Zhou, A. Wanga, S. C. Wu, J. Sun, S. Park and T. N. Jackson, *Appl. Phys. Lett.* **88**, 083502 (2006)

[31] K. Tsukagoshi, J. Tanabe, I, Yagi, K, Shigeto, K, Yanagisawa and Y. Aoyagi, *J. Appl. Phys.* **99**, 064506, (2006)

[32] S. J. Mun, J. M. Choi, K. H. Lee, K. Lee and S. Im, *Appl. Phys, Lett.*, **93**, 233301, (2008).

[33] C. D. Dimitrakopoulos, P. R. L. Malenfant, adv. Mater., **14**, 99 (2002).

[34] A. Dodabalapur, L. Torsi, H. E. Katz, *Science* **268**, 270, (1995)

[35] A. C. Mayer, M. L. Swiggers, C. J. Johnson, J. L. Mack, Z. T. Zhu, R. L. Headrick, G. G. Malliaras, *Thin Film Transistor Technologies,* 288, (2002)

[36] S. R. Forrest, *Chem. Rev.*, **97**, 1793, (1997).

[37] M. Pfeiffer, A. Beyer, T. Fritz and K. Leo, *Appl. Phys. Lett.,* **73**, 3202, (1998).

---

[38] B. Maennig, M. Pfeiffer, A. Nollau, X. Zhou, K. Leo and P. Simon, *Phys. Rev. B*, **64**, 195208, (2001).

[39] G. Horowitz, M. E. Hajlaoui and R. Hajilaoui, *J. Appl. Phys.* , **87**, 4456, (2000).

[40] A. J. Maliakal, J. Y. C. Chen, W. Y. So, S. Jockusch, B. Kim, M. F. Ottaviani, A. Modelli, N. J. Turro, C. Nuckolls and A. P. Ramirez, *Chem. Mater.,* **21**, 5519, (2009).

41 M. Haemori, J. Yamaguchi, S. Yaginuma, K. Itaka and H. Koinuma, *Jpn J. Appl. Phys.*, **44**, 3740, (2005).

[42] R. Ruiz, A. Papadimitratos, A. C. Mayer, G. G. Malliaras, *Adv. Mater.* 17, 1798 (2005)

43 M. Haemori, J. Yamaguchi, S. Yaginuma, K. Itaka and H. Koinuma: *Jpn J. Appl. Phys.*, **44**, (2005), 3740.

[44] S Pratontep, M Brinkmann, F Nüesch, L Zuppiroli - *Synthetic Metals*, **146, (**2004), 3

[45] R. G. Breckenridge, and W. R. Hosler, *Phys. Rev.* **91**, 4, (1953)

46 I. Terasaki, Y. Sasago, and K. Uchinokura, *Phys. Rev. B*, **56** [20] R12685 ‑ 7 (1997).

[47] Y. Wang, N. S. Rogado, R. J. Cava, and N. P. Ong, *Nature*, **423** [6938] 425–

---

8 (2003).

[48] I. Tsuyumoto, T. Hosono, M. Murata, *J. Amer. Cera. Soc.* **7,** 89, (2006)

[49] N. Okinaka and T. Akiyama, *Jpn. J. Appl. Phys.*, **45**, 7009 (2006).

[50] Q. Y. He, Q. Hao, G. Chen, B. Poudel, X. W.i Wang, D. Z. Wang, and Z. F. Ren, *Appl. Phys. Lett.* **91**, 052505 (2007)

[51] L. R. Sheppard, T. Bak, and J. Nowotny, *J. Phys. Chem. C*, **112**, 611, (2008)

[52] L. D. Hicks, T. C. Harman, X. Sun, M. S. Dresselhaus, *Phys. Rev. B: Condens. Matter Mater. Phys.* ***53***, R10493. (1996)

[53] J. Heremans, in *Thermoelectric Materials 2003—Research and Applications,MRS Symp. Proc*. (Eds: G. S. Nolas, J. Yang, T. P. Hogan, D. C. Johnson), Materials Research Society Press, Pittsburgh, PA 2004, pp. 3–14.

[54] T. Koga, S. B. Cronin, M. S. Dresselhaus, in *Thermoelectric Materials—The Next Generation Materials for Small-Scale Refrigeration and Power Generation Applications, MRS Symp.* (Eds: T. M. Tritt,G. S. Nolas, G. Mahan, M. G. Kanatzidis, D. Mandrus), Materials Research Society Press, Pittsburgh, PA, 2000, pp. Z4.3.1–4.3.6.

---

[55] M. S. Dresselhaus, G. Chen, M. Y. Tang, R. Yang, H. Lee, D. Wang, Z. Ren, J. P. Fleurial, and P. Gogna, *Adv. Mater.* **19,** 1043, (2007)

[56] Y. M. Lin, S. B. Cronin, J. Y. Ying, M. S. Dresselhaus, J. P. Heremans, *Appl. Phys. Lett.* **2000**, *76,* 3944.

[57] T. Koga, S. B. Cronin, M. S. Dresselhaus, J. L. Liu, K. L. Wang, *Appl. Phys. Lett.* **2000**, *77*, 1490.

[58] a) G. Chen, *Phys. Rev. B: Condens. Matter Mater. Phys.* **1998**, *57*, 14 958. b) G. Chen, in *Proc. 1996 Int. Mech. Eng. Congress*, Vol. 59, AMSE, New York, **1996**, pp. 13–23.

[59] M Paulose, K Shankar, S Yoriya, H. E. Prakasam, O. K. Varghese, G. K. Mor, T. A. Latempa, A. Fitzgerald and C. A. Grimes, *J. Phys. Chem. B* 110 16179, 2006

[60] H. Foll, S. Langa, J. Carstensen, M. Christophersen and I. M. Tiginyanu, *Adv. Mater.* 15 183–98, 2003

[61] G.K. Mor, K. Shankar, M. Paulose, O.K. Varghese, C.A. Grimes, *Nano Lett*. **5** 191 (2005).

[62] Y. Y. Zhang, W. Y. Fu, H B. Yang, Q Qi, Y. Zeng, T. Zhang, R. X. Ge, G. T. Zhou, *Applied Surface Science* **254**, 5545–5547, (2008)

---

[63] K. Shankar, G. K. Mor, H. E. Prakasam, S. Yoriya, M. Paulose, O. K. Varghese and C. A. Grimes, *Nanotechnology*, **18,** 065707, (2007)

[64] Zhenjun Wang, Wendong Wang, and Jinke Tang, Le Duc Tung, Leonard Spinu, and Weilie Zhou, *Applied Physics Letters* **83**, 518 (2003).

[65] Ana M. Ruiz, Go Sakai, Albert Cornet, Kengo Shimanoe,Joan Ramon Morante, Noboru Yamazoe, *Sensors and Actuators B,* **93,** 509–518 (2003)

[66] Y. Li, W. Wlodarski, K. Galatsis, S.H. Moslih, J. Cole, S. Russo, N.Rockelmann, *Sensors and Actuators B* **83**, 160–163 (2002)

[67] A. Ruiz, A. Cornet, G. Sakai, K. Shimanoe, J.R. Morante, N.Yamazoe, *Chem. Lett.* **9,** 892–893 (2002)

[68] J. L. Zhao, X. H. Wang, T. Y. Sun and L. T. Li, *Nanotechnology*, **16**, 2450 (2005)

[69] J. He, R.K. Behera, M.W. Finnis, X. Li, E.C. Dickey, S.R. Phillpot, S.B. Sinnott, *Acta Materialia* **55** (2007) 4325–4337

[70] F. A. Kroger, *The Chemisty of Imperfect Crystals*, Vol. 2, p. 40, American Elsevier Publishing Corporation, New York (1974).

---

[71] G. Gustafsson, Y. Cao, G. M. Treacy, F. Klavetter, N. Colaneri and A. J. Heeger, *Lett. to Nat.*, **357**, 477, (1992)

[72] A. A. Efremov, N. I. Bochkareva, R. I. Gorbunov, D. A. Lavrinovich, Yu. T. Rebane, D. V. Tarkhin and Yu. G. Shreter, *Semiconductors*, **40,** 5, (2006)

73 X. A. Cao and S. D. Arthur, Appl. Phys. Lett., 85, 18, (2004)

[74] N. Wang, C. H. Wang, J. X. Lei and D. S. Zhu, *Electronic Packaging Technology & High Density Packaging, 2009. ICEPT-HDP '09. International Conference*, 10-13 Aug. 2009, pp.433

[75] N. Wang, C. H. Wang, Jun-xi Lei, D. S. Zhu, *2009 International Conference on Electronic Packaging Technology & High Density Packaging (ICEPT-HDP),* 437

[76] D. Wang, L. Tang, M. Long and Z. Shuai, *J. Chem. Phys.*, **131,** 224704, (2009)

[77] G. K. Madsen, *J. Am. Chem. Soc.* **128,** 12140, (2006)

[78] J. Yang, H. M. Li, T. Wu, W. Q. Zhang, L. D. Chen, and J. H. Yang, *Adv. Funct. Mater.*, **18,** 2880, (2008)

---

[79] H. Beyer J. NurnusH. BöttnerA. LambrechtE. Wagner and G. Bauer, *Physica E: Low-dimensional Systems and Nanostructures,* **13,** 965 (2002)

[80] F. J. DiSalvo, *Science,* **285,** 703, (1999)

[81] C. K. Lu and H. F. Meng, *Phys. Rev. B,* **75,** 235206 (2007)

[82] S. Ogawa, T. Naijo, Y. Kimura, H. Ishii and M. Niwano, *Appl. Phys. Lett.,* **86,** 202104 (2005)

[83] M. L. Chabinyc, R. A. Street and J. E. Northrup, *Appl. Phys, lett.,* **90,** 123508 (2007)

[84] V. I. Arkhipov, E. V. Emelianova, Y. H. Tak and H. Bassler, *J. Appl. Phys.*, **84**, 2, (1998)

[85] K. P. Pernstich, S. Haas, D. Oberhoff, C. Goldmann, D. J. Gundlach, B. Batlogg, A. N. Rashid and G. Schitter, *J. Appl. Phys*., **96**, 11 (2004)